

Paleocene to Pliocene low-latitude, high-elevation basins of southern Tibet: Implications for tectonic models of India-Asia collision, Cenozoic climate, and geochemical weathering

Miquela Ingalls^{1†}, David Rowley¹, Gerard Olack¹, Brian Currie², Shanying Li², Jennifer Schmidt³, Marissa Tremblay^{4,5}, Pratigya Polissar⁶, David L. Shuster^{4,5}, Ding Lin⁷, and Albert Colman¹

¹Department of the Geophysical Sciences, The University of Chicago, Chicago, Illinois 60637, USA

²Department of Geology & Environmental Earth Science, Miami University, Oxford, Ohio 45055, USA

³Department of Earth & Environmental Sciences, Lehigh University, Bethlehem, Pennsylvania 18015, USA

⁴Department of Earth & Planetary Science, University of California, Berkeley, California 94720, USA

⁵Berkeley Geochronology Center, 2455 Ridge Road, Berkeley, California 94709, USA

⁶Lamont-Doherty Earth Observatory of Columbia University, 61 Route 9W, Palisades, New York 10964, USA

⁷Institute for Tibetan Plateau Research, Chinese Academy of Sciences, Beijing, People's Republic of China

ABSTRACT

The elevation history of the Tibetan Plateau promises insight into the mechanisms and dynamics that develop and sustain high topography over tens of millions of years. We present the first nearly continuous Cenozoic elevation history from two sedimentary basins on the southern Tibetan Plateau within the latest Cretaceous to Eocene Gangdese arc. Oxygen-isotope and Δ_{47} clumped-isotope compositions of nonmarine carbonates allow us to constrain carbonate formation temperature and reconstruct the paleoprecipitation record of the Eocene to Pliocene Oiyug Basin and Paleocene to Eocene Penbo Basin. We exploit the systematic decrease of surface temperature and meteoric water $\delta^{18}\text{O}$ values with elevation to derive paleoelevation estimates for these basins. Minimally altered and unaltered pedogenic and lacustrine carbonates from the Oiyug Basin yield $\Delta_{47, \text{CDES}}$ (relative to the carbon dioxide equilibrium scale [CDES]) values of 0.625‰ to 0.755‰, which correspond to temperatures of 1–30 °C using a Δ_{47} thermometer for low-temperature carbonates. Similarly, the Penbo Basin yielded $\Delta_{47, \text{CDES}}$ values of 0.701‰ to 0.726‰, corresponding to temperatures of 6–12 °C. The apparent evidence for survival of primary clumped-isotope values in the face of substantial burial and heating is an important

result for the field of carbonate clumped-isotope thermometry.

Our paleoelevation estimates for the Eocene to Pliocene Oiyug Basin (~6.5–4.1 km) support previous evidence that high elevations were attained in southern Tibet by at least ca. 30 Ma. Stable-isotope results allow for the possibility of significant topographic subsidence during the Miocene as a result of regional extension. In the Penbo Basin, our paleoelevation estimates for the Paleocene to Eocene Nianbo Formation (4.4 +1.3/–1.7 km) and Eocene Pana Formation (4.1 +1.2/–1.6 km) extend the altitude record of the southern Tibetan Plateau to pre-India-Asia collision. These results support the “Lhasaplano” model of an Andean-type continental margin tectonic system.

The rise of the Himalayas and Tibet is often invoked to understand isotopic proxies for global chemical weathering in the Cenozoic and has constrained the debate on the nature of CO_2 –climate–weathering feedbacks. The nature of the Tibetan paleoelevations from pre- to postcollision, as presented here, indicates that high relief at low latitude prevailed on the Asian margin much earlier than previously thought. Thus, high topography alone at low latitude is not sufficient to account for the Cenozoic weathering proxy record.

INTRODUCTION

The debate over when and how the largest and highest plateau on Earth reached its current

altitude is reframed here in the context of recent evidence for an older onset of India-Eurasia collision. This has important implications for tectonics (Le Pichon et al., 1992; Kapp et al., 2007), crustal mass balance considerations (Ingalls et al., 2016), and feedbacks among tectonics, weathering, climate, and the global carbon cycle (e.g., Raymo and Ruddiman, 1992).

Recent efforts have established an age of onset of the India-Eurasia continental collision of ca. 58 Ma from the Indian deep-water, off-shelf passive continental margin environment represented by Eocene strata near Sangdanlin in south-central Tibet (DeCelles et al., 2014; Hu et al., 2015). Ingalls et al. (2016) used these and other data to suggest an age of ca. 56 ± 2 Ma for collision of thicker (>20 km) continental crust in the vicinity of Sangdanlin, a younger age of ca. 51 Ma in the Zanskar region farther west (Gaetani and Garzanti, 1991; Green et al., 2008), and an essentially unconstrained ca. 54 ± 4 Ma age nearer to the eastern syntaxis.

Our study of the tectonic history of Penbo and Oiyug Basins provides a framework for the land surface evolution of the southern margin of Eurasia and the sedimentary basins associated with the Linzizong volcanic arc and younger sedimentary basins during the Cenozoic collisional history spanning ca. 55 Ma to ca. 5 Ma. We obtained $\delta^{18}\text{O}_c$ measurements on lacustrine, pedogenic, and groundwater calcites from both basins. We used the clumped-isotope-derived mineral formation temperatures from a subset of the calcite samples to calculate the original oxygen isotopic composition of meteoric water

[†]ingalls@uchicago.edu.

($\delta^{18}O_w$) from $\delta^{18}O_c$ measurements. Finally, we assessed alteration and secondary calcite precipitation with careful petrographic analyses and characterization of possible diagenesis coupled with our clumped-isotope results.

The Oiyug Basin sedimentary record spans nearly the entire Cenozoic, making it a unique site for reconstructing the elevation history of the southern part of the Tibetan Plateau (Fig. 1). Previous paleoaltimetry studies of the basin included paleoenthalpy-derived estimates of ca. 15 Ma elevations from floral physiognomy (Spicer et al., 2003; Khan et al., 2014), oxygen-isotope–based estimates from carbonate minerals (Currie et al., 2005, 2016), and compound-specific δD of leaf wax *n*-alkanes (Currie et al., 2016). These studies have progressively added archives as a means of testing new proxies and validating prior reconstructions of past hypsometry and environmental conditions. We provide new stable-isotope data from Paleogene nonmarine carbonates to extend the temporal range of the isotopic record in the Oiyug Basin.

Additionally, we present clumped-isotope estimates of carbonate formation temperatures to better constrain paleowater isotopic compositions for samples previously analyzed by Currie et al. (2016). These data thus help to remove bias in paleoelevation estimates through assumptions regarding carbonate–water fractionation temperatures.

The clumped-isotope paleothermometry and stable-isotope paleoaltimetry results presented here support the existence of an Andean-type continental arc on the southern margin of Eurasia with elevations >4.1 km at the onset or just prior to the onset of the India and Eurasia collision in the Penbo-Linzhou region near Lhasa, Tibet. We also advance the elevation record of the Oiyug Basin, ~160 km west of Lhasa, into the Eocene and provide additional support that the Oiyug Basin was high throughout the Oligocene to Pliocene, building on the work of Currie et al. (2016). Our high paleoelevations agree with aspects of the “Lhasaplano” model (Kapp et al., 2007), including a high-standing Lhasa

terrane before India-Asia collision, and provide additional evidence against models invoking en masse (England and Houseman, 1986; Harrison et al., 1992, 1995; Molnar et al., 1993) or local plateau uplift (Wang et al., 2006) from significantly lower elevations in the Neogene.

Stable-Isotope Palealtimetry in the India-Asia Collision Zone

Numerous investigations have reconstructed the elevation history of the Himalayas and Tibetan Plateau using the oxygen-isotopic composition of nonmarine carbonates (Garzzone et al., 2000; Rowley et al., 2001; Currie et al., 2005; Rowley and Currie, 2006; DeCelles et al., 2007; Quade et al., 2007; Saylor et al., 2009; Ding et al., 2014; Huntington et al., 2015). The isotopic composition of the carbonate minerals relates to that of the water from which they precipitated, which in turn depends upon the composition of meteoric water falling in the drainage basin. Paleoelevation estimates then derive from the

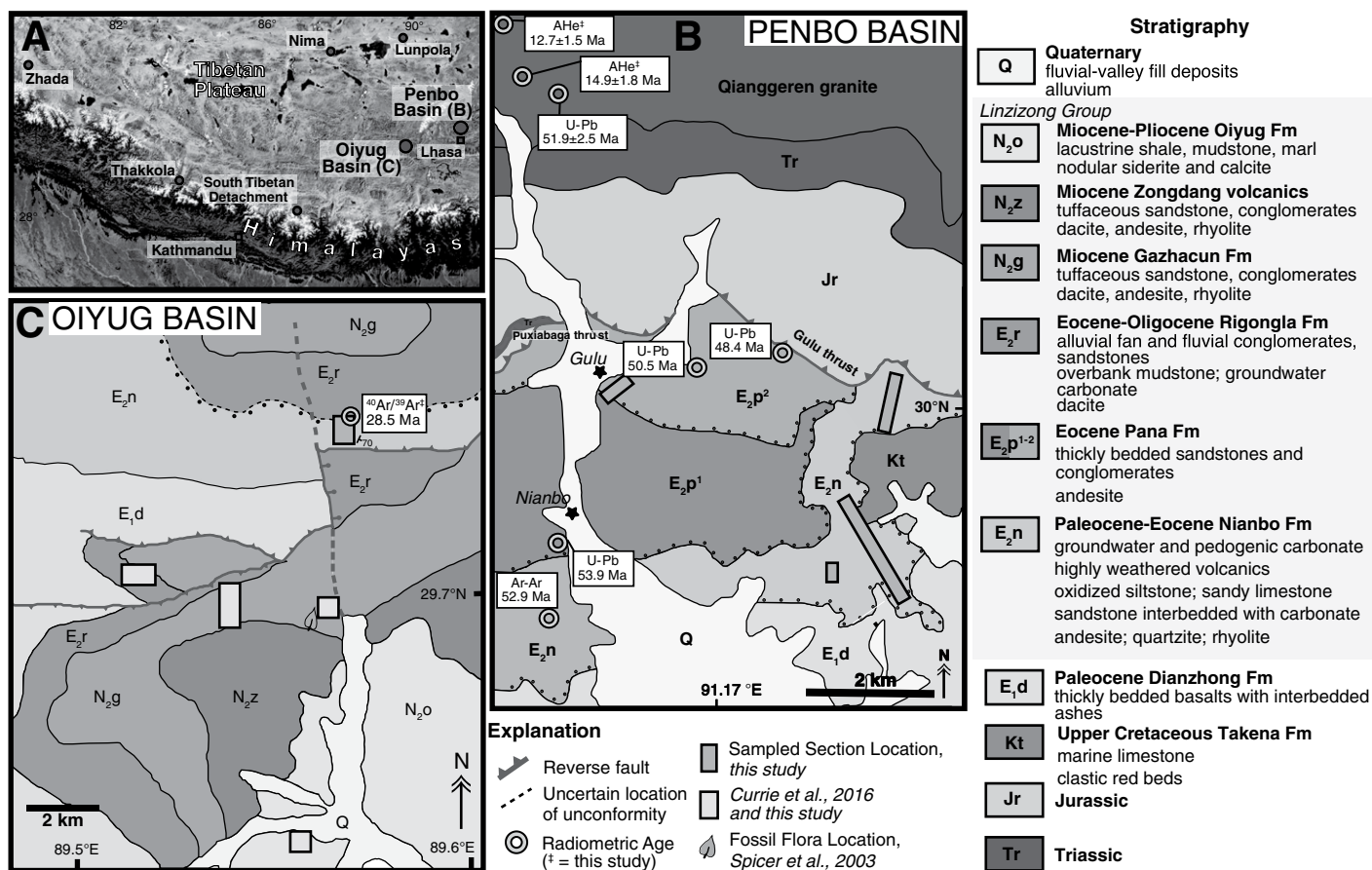


Figure 1. Maps of the sampled regions. (A) Regional Landsat image of the Tibetan Plateau (adapted from Currie et al., 2016). (B) Geologic map of the Linzhou-Penbo region, including the Nianbo type section. Map is based on and geochronology is sourced from Ding et al. (2014) and He et al. (2007). (C) Geologic map of the Oiyug Basin displaying measured section locations from Currie et al. (2016; gray) and this study (blue). The fossil floral locality of Spicer et al. (2003) is depicted as a leaf.

sensitive relationship between elevation and the isotopic value of precipitation in low-latitude (<35°) orographic systems (Rowley and Garzzone, 2007; Rowley, 2007). This connection is predicted based on atmospheric thermodynamic modeling of the expected isotopic lapse rate for water vapor and precipitation and has been verified by modern observations (Rowley et al., 2001; Rowley and Garzzone, 2007; Rowley, 2007). The primary determinants of the $\delta^{18}\text{O}_w$ -elevation relationship are the temperature (T) and relative humidity (RH) of the starting air mass. Rowley et al. (2001) used National Centers for Environmental Prediction (NCEP) reanalysis output of modern global monthly mean data over entirely oceanic, low-latitude (<35°) regions to compute the probability density function of T and RH (Kalnay et al., 1996). Each starting T and RH pair populates a unique vertical trajectory through isotopic composition and elevation space. The sets of these vertical trajectories define the expected isotopic compositions of low-latitude atmospheric vapor and use empirical fitting to the frequency distribution of isotopic composition of precipitation as a function of elevation. Model elevations are calculated using a quartic function that describes the relationship between elevation and $\Delta(\delta^{18}\text{O}_p)$, where $\Delta(\delta^{18}\text{O}_p)$ is the difference between the oxygen-isotope composition of precipitation at sea level and that at high altitude. This function is the condensation-weighted mean polynomial fit to an ~33,000 iteration regression of 40 yr of monthly global mean T and RH data:

$$\begin{aligned} \text{Elevation (m)} = & -0.0155[\Delta(\delta^{18}\text{O}_p)]^4 - \\ & 1.1302[\Delta(\delta^{18}\text{O}_p)]^3 - 33.939[\Delta(\delta^{18}\text{O}_p)]^2 - \\ & 642.71[\Delta(\delta^{18}\text{O}_p)]. \end{aligned} \quad (1)$$

This model was assessed by sampling modern stream waters in the Himalaya to central Tibet, calculating $\Delta(\delta^{18}\text{O}_p)$, and comparing their predicted elevations with the actual modern elevations. This isotopic method yielded reasonable fits to these data sets (Rowley et al., 2001; Currie et al., 2005; Rowley and Currie, 2006; Rowley and Garzzone, 2007; Hren et al., 2009). There is some tendency of the model to underestimate elevations rather than overestimate, suggesting that it is likely a conservative proxy for past elevations. Further discussion of the paleoaltimetry model parameters can be found in the Appendix.¹

The Siwalik Group is favored as an archive for low-latitude, near-sea-level climate conditions in the Neogene, because both carbon- and oxygen-isotope compositions are interpreted to be primary (Quade et al., 1995; Quade and Cerling, 1995), and there exists excellent control on depositional age and burial history. We calculated

$\Delta(\delta^{18}\text{O}_p)$ using the mean low-elevation $\delta^{18}\text{O}_w$ value determined from 12 to 2.5 Ma paleosol carbonates (1–5 cm diameter) of the Siwalik Group in Pakistan and Nepal (Quade and Cerling, 1995; Quade et al., 2013). The Siwalik carbonates are presumed to have precipitated in near-isotopic equilibrium from soil water, which is closely related to meteoric water. Temperature- and mineral-specific fractionation factors ($\alpha_{\text{CO}_2\text{-H}_2\text{O}}$) were used to derive paleosurface or paleogroundwater composition ($\delta^{18}\text{O}_w$) from carbonate isotopic values ($\delta^{18}\text{O}_c$). We calculated $\delta^{18}\text{O}$ values of water in the mineralizing solution (Tables 1 and 2) using fractionation equations for calcite (Kim and O'Neil, 1997), dolomite (Vasconcelos et al., 2005), and siderite (Zhang et al., 2001), which were calculated using the average temperatures derived from Δ_{47} clumped isotopes for each geologic unit. The dominant controls on $\delta^{18}\text{O}_c$ values of unaltered to minimally altered carbonate are the extent of Rayleigh distillation of water vapor in the air masses that deliver precipitation to the region, which scales with elevation (Dansgaard, 1954), and the extent of evaporative ^{18}O enrichment. An assessment of evaporative enrichment is incorporated into our presentation of the isotopic data.

Previously derived $T(\Delta_{47})$ values for paleosols from the upper 2.5 km (<5.5 Ma) of the Siwalik Group at Surai Khola in Nepal were <34 °C (Quade et al., 2013). Although the deposits older than 5.5 Ma experienced greater burial depths and yielded higher $T(\Delta_{47})$, Quade et al. (2013) argued that the Surai Khola sedimentary package is rock-buffered and has undergone little recrystallization, and therefore $\delta^{18}\text{O}_c$ is preserved. The average $\delta^{18}\text{O}_c$ value of the Neogene Siwaliks is -7.4‰ (relative to Vienna Pee Dee belemnite [VPDB]; Quade et al., 2013). Due to the extent of Δ_{47} alteration during burial in Surai Khola, we did not use the clumped-isotope-derived temperatures from deposits older than 5.5 Ma for the calculation of $\delta^{18}\text{O}_w$ from $\delta^{18}\text{O}_c$. Instead, we used a low-elevation warm month mean temperature (WMMT) of 28.1 ± 3.4 °C derived from a Climate Leaf Analysis Multivariate Program (CLAMP) analysis of two Lower Siwalik mid-Miocene two fossil flora assemblages (Khan et al., 2014). We assigned a $\delta^{18}\text{O}_w$ value of $-6.6\text{‰} \pm 2.8\text{‰}$ (relative to Vienna stan-

dard mean ocean water [VSMOW]) as our low-elevation precipitation isotopic value ($\delta^{18}\text{O}_w$) in the Miocene and older sediments and $-4.6\text{‰} \pm 1.4\text{‰}$ VSMOW to the Pliocene sediments to account for climate change during the Cenozoic. Error was propagated through the paleoelevation model using the sum in quadrature of the uncertainties associated with calculating mean $\delta^{18}\text{O}_w$ values for each sample, as well as the $2\sigma \Delta_{47}$ uncertainty.

Case for Multiple Proxies in Reconstructions of Ancient Topography and Environments

Carbonate stable-isotope paleoaltimetry depends critically on the preservation of a primary $\delta^{18}\text{O}_c$ signal in the variably altered rocks preserved in collisional zones. Primary carbonate isotopic compositions are prone to alteration and diagenetic resetting by deep burial (Leier et al., 2009), which can shift $\delta^{18}\text{O}_c$ to lower values, eliminating the possibility of constraining elevation history using the stable-isotope record (Garzzone et al., 2004; Leier et al., 2009). Such a lowering of $\delta^{18}\text{O}_c$ would result in an incorrectly high paleoelevation interpretation (Garzzone et al., 2004). We employed petrography, vitrinite reflectance, thermochronometric data, and clumped-isotope thermometry to assess alteration and rule out the use of isotopic data from thermally mature samples in paleoelevation reconstructions.

The exploitation of multiple paleoelevation and paleoenvironmental proxies in a single stratigraphic package allows for calibration and checks among conventional archives. Currie et al. (2016) conducted such a study in the Oiyug Basin, characterizing ~30 m.y. of relative elevation stasis in the evolving depositional environment of the Oiyug Basin. Currie et al. (2016) synthesized multiple proxies for paleo-meteoric water ($\delta^{18}\text{O}_{\text{FeCO}_3}$, $\delta^{18}\text{O}_{\text{CaCO}_3}$, $\delta\text{D}_{\text{leaf wax}}$) to provide mid-Miocene (5.1 km +1.3/–1.9 km) and late Oligocene to mid-Miocene (4.1 km +1.2/–1.6 km) paleoelevation estimates of this region, offering a unique opportunity for testing the fidelity of other stable-isotope proxies. Khan et al. (2014) determined a mid-Miocene (ca. 15 Ma) paleoelevation of 5.54 ± 0.73 km by reevaluating paleo-enthalpy estimates for a fossil flora locality (Spicer et al., 2003) in the Oiyug Basin relative to new fossil flora localities in the Siwaliks, which they used as their sea-level proxy.

Clumped isotopes can be powerful in studying the evolution of ancient land surfaces when the original isotopic signature is preserved (Ghosh et al., 2006b; Quade et al., 2007). In this study, we applied calcite Δ_{47} -derived formation temperatures ($T[\Delta_{47}]$; Table 3) to previously

¹GSA Data Repository item 2017300, an appendix, supplemental figures of $^{40}\text{Ar}/^{39}\text{Ar}$ data and evaporative trend in $\delta^{18}\text{O}$ by mineralogy, and Δ_{47} data tables containing measurements of calcite standards. The appendix text outlines quality control tests and corrections performed on Δ_{47} measurements, and paleoaltimetry model parameters, is available at <http://www.geosociety.org/datarepository/2017> or by request to editing@geosociety.org.

TABLE 1. STABLE-ISOTOPE DATA FOR ALL CARBONATES AND CALCULATED PALEOELEVATIONS OF THE PENBO BASIN

Sample	Carbonate type	Location in section (m)	$\delta^{13}\text{C}$ (‰, VPDB)	$\delta^{18}\text{O}_c$ (‰, VPDB)	$T(\Delta_{47})$ (°C \pm 5 °C):			Mean $\delta^{18}\text{O}_w$ ($\pm 2.2\%$)	$\Delta(\delta^{18}\text{O}_w)$ (‰)	Model elevation (km \pm 2 σ)
					Lacustrine carbonate	10.2 °C	15.2 °C			
					α (calcite-H ₂ O):					
					Pedogenic carbonate					
					$T(\Delta_{47})$ (°C \pm 5 °C):					
					α (calcite-H ₂ O):					
Pana Formation										
483C	Lacustrine limestone	300	-7.6	-13.9	-14.7	-13.6	-15.8	-14.7 \pm 2.2	-10.1	3.9 +1.1/-1.3
484A	Lacustrine limestone	300	-7.2	-14.0	-14.9	-13.8	-16.0	-14.9 \pm 2.2	-10.3	4.0 +1.1/-1.3
483D	Lacustrine limestone	300	-6.3	-14.3	-15.2	-14.1	-16.3	-15.2 \pm 2.2	-10.6	4.0 +1.2/-1.3
483B	Lacustrine limestone	300	-7.5	-14.7	-15.5	-14.4	-16.6	-15.5 \pm 2.2	-10.9	4.5 +1.3/-1.6
483A	Lacustrine limestone	300	-7.3	-14.8	-15.6	-14.5	-16.7	-15.6 \pm 2.2	-11.0	4.5 +1.3/-1.7
491B	Groundwater calcite nodule	300	-6.6	-13.1	-14.8	-14.4	-15.2	-14.8 \pm 0.8	-8.2	3.9 +1.0/-1.5
491C	Groundwater calcite nodule	300	-5.8	-11.7	-13.4	-13.0	-13.8	-13.4 \pm 0.8	-6.8	3.4 +0.8/-1.3
490A	Paleosol carbonate nodule	300	-7.6	-14.1	-15.8	-15.4	-16.2	-15.8 \pm 0.8	-9.2	4.1 +1.1/-1.6
490B	Paleosol carbonate nodule	300	-7.2	-13.6	-15.2	-14.8	-15.7	-15.2 \pm 0.8	-8.6	4.0 +1.1/-1.5
491A	Paleosol carbonate nodule	300	-6.1	-11.7	-13.4	-13.0	-13.8	-13.4 \pm 0.8	-6.8	3.4 +0.8/-1.3
475B	Lacustrine limestone	275	-3.2	-13.7	-14.5	-13.5	-15.7	-14.6 \pm 2.2	-10.0	4.3 +1.3/-1.5
475C	Lacustrine limestone	275	-3.8	-14.4	-15.2	-14.2	-16.4	-15.3 \pm 2.2	-10.7	4.5 +1.3/-1.6
475D	Lacustrine limestone	275	-4.5	-15.4	-16.2	-15.1	-17.3	-16.2 \pm 2.2	-11.6	4.7 +1.4/-1.7
475A	Lacustrine limestone	275	-4.1	-16.1	-16.9	-15.8	-18.0	-16.9 \pm 2.2	-12.3	4.8 +1.4/-1.8
Mean elevation (km)*										4.1 +1.2/-1.6
Nianbo Formation										
446C	Lacustrine limestone	236	-2.7	-16.7	-17.5	-16.5	-18.7	-17.6 \pm 2.2	-13.0	4.9 +1.4/-1.8
446H	Lacustrine limestone	235	-2.2	-17.9	-18.7	-17.7	-19.9	-18.7 \pm 2.2	-14.1	5.1 +1.4/-1.9
446D	Paleosol carbonate nodule	234	-4.6	-17.3	-18.9	-18.5	-19.4	-18.9 \pm 0.8	-12.3	4.8 +1.3/-1.9
446F	Lacustrine limestone	232	-3.5	-16.1	-16.9	-15.8	-18.0	-16.9 \pm 2.2	-12.3	4.8 +1.4/-1.8
446E	Lacustrine limestone	232	-3.2	-17.3	-18.1	-17.0	-19.2	-18.1 \pm 2.2	-13.5	5.0 +1.4/-1.9
447A	Paleosol carbonate nodule	222	-3.8	-19.0	-20.7	-20.3	-21.1	-20.7 \pm 0.8	-14.1	5.1 +1.4/-2.0
448C	Lacustrine limestone	215	-3.8	-12.7	-13.5	-12.4	-14.6	-13.5 \pm 2.2	-8.9	4.0 +1.2/-1.4
448A	Lacustrine limestone	215	-3.9	-12.0	-12.8	-11.7	-13.9	-12.8 \pm 2.2	-8.2	3.9 +1.1/-1.3
448E	Lacustrine limestone	214	-4.8	-11.4	-12.2	-11.1	-13.3	-12.2 \pm 2.2	-7.6	3.7 +1.1/-1.2
448D	Lacustrine limestone	214	-4.0	-12.0	-12.8	-11.7	-13.9	-12.8 \pm 2.2	-8.2	3.9 +1.1/-1.3
448	Lacustrine limestone	214	-3.5	-15.3	-16.2	-15.1	-17.3	-16.2 \pm 2.2	-11.6	4.7 +1.4/-1.7
P0929-c	Lacustrine limestone	208	-3.3	-12.7	-13.1	-11.9	-14.4	-13.1 \pm 2.5	-8.6	4.0 +1.2/-1.3
DL104-3b	Lacustrine limestone	200	-2.5	-12.4	-13.6	-12.5	-14.7	-13.6 \pm 2.2	-9.0	4.1 +1.2/-1.4
451B	Paleosol carbonate nodule	188	-2.7	-15.3	-17.0	-16.6	-17.4	-17.0 \pm 0.8	-10.4	4.4 +1.2/-1.7
452A	Lacustrine limestone	186	-4.0	-10.9	-11.7	-10.7	-12.9	-11.8 \pm 2.2	-7.2	3.5 +1.0/-1.1
452B	Lacustrine limestone	183	-3.7	-12.3	-13.1	-12.0	-14.3	-13.1 \pm 2.2	-8.6	4.0 +1.2/-1.3
452D	Lacustrine limestone	183	-3.5	-15.0	-15.8	-14.8	-17.0	-15.9 \pm 2.2	-11.3	4.6 +1.4/-1.7
452C	Paleosol carbonate nodule	181	-3.2	-14.8	-16.4	-16.0	-16.8	-16.4 \pm 0.8	-9.8	4.3 +1.2/-1.7
452G1	Lacustrine limestone	180	-3.5	-11.8	-13.5	-13.1	-13.9	-13.5 \pm 0.4	-6.9	3.5 +0.9/-1.3
452G3	Groundwater calcite nodule	180	-4.2	-16.0	-17.7	-17.2	-18.1	-17.7 \pm 0.4	-11.1	4.6 +1.3/-1.8
452E	Groundwater calcite nodule	179	-3.9	-13.8	-15.5	-15.0	-15.9	-15.5 \pm 0.4	-8.9	4.0 +1.1/-1.6
514	Lacustrine limestone	170	-2.1	-15.1	-15.9	-14.8	-17.0	-15.9 \pm 2.2	-11.3	4.6 +1.4/-1.7
514A	Lacustrine limestone	170	-2.0	-15.2	-16.0	-14.9	-17.1	-16.0 \pm 2.2	-11.4	4.6 +1.4/-1.7
511	Lacustrine limestone	170	-0.1	-21.8	-22.6	-21.5	-23.7	-22.6 \pm 2.2	-18.0	5.7 +1.5/-2.1
440D	Lacustrine limestone	164	-4.5	-16.3	-17.1	-16.0	-18.3	-17.1 \pm 2.2	-12.5	4.9 +1.4/-1.8
440B	Paleosol carbonate nodule	162	-3.8	-17.2	-18.9	-18.5	-19.3	-18.9 \pm 0.8	-12.3	4.8 +1.3/-1.9
505	Lacustrine limestone	150	-0.2	-17.3	-18.1	-17.0	-19.2	-18.1 \pm 2.2	-13.5	5.0 +1.4/-1.9
508	Lacustrine limestone	140	-3.8	-12.3	-13.1	-12.0	-14.2	-13.1 \pm 2.2	-8.5	3.9 +1.2/-1.3
439E	Paleosol carbonate nodule	129	-4.6	-15.8	-17.5	-17.1	-17.9	-17.5 \pm 0.8	-10.9	4.5 +1.2/-1.8
439D	Groundwater calcite nodule	127	-4.3	-16.3	-18.0	-17.6	-18.4	-18.0 \pm 0.8	-11.4	4.6 +1.3/-1.8
456	Lacustrine limestone	122	-3.7	-15.5	-16.3	-15.2	-17.4	-16.3 \pm 2.2	-11.7	4.7 +1.4/-1.7
504A	Lacustrine limestone	120	-0.7	-17.8	-18.6	-17.5	-19.7	-18.6 \pm 2.2	-14.0	5.1 +1.4/-1.9
439	Groundwater calcite nodule	120	-5.2	-15.6	-17.3	-16.9	-17.7	-17.3 \pm 0.8	-10.7	4.5 +1.2/-1.8
439C	Paleosol carbonate nodule	120	-5.4	-15.5	-17.2	-16.8	-17.6	-17.2 \pm 0.8	-10.6	4.5 +1.2/-1.8
523	Paleosol carbonate nodule	105	-3.4	-16.3	-17.9	-17.5	-18.4	-18.0 \pm 0.8	-11.4	4.6 +1.3/-1.8
512	Paleosol carbonate nodule	100	-3.5	-15.1	-16.8	-16.3	-17.2	-16.8 \pm 0.8	-9.6	4.2 +1.2/-1.4
534A	Paleosol carbonate nodule	100	-5.8	-14.5	-16.1	-15.7	-16.6	-16.1 \pm 0.8	-9.5	4.2 +1.1/-1.7
534C	Paleosol carbonate nodule	100	-5.3	-15.4	-17.1	-16.7	-17.5	-17.1 \pm 0.8	-10.5	4.4 +1.2/-1.7
534D	Paleosol carbonate nodule	100	-6.7	-12.8	-14.5	-14.1	-14.9	-14.5 \pm 0.8	-7.9	3.8 +1.0/-1.5
534F	Paleosol carbonate nodule	100	-3.3	-14.3	-16.0	-15.6	-16.4	-16.0 \pm 0.8	-9.4	4.2 +1.1/-1.6
534G	Paleosol carbonate nodule	100	-2.8	-16.3	-17.9	-17.5	-18.3	-17.9 \pm 0.8	-11.3	4.6 +1.1/-1.6
534I	Paleosol carbonate nodule	100	-4.5	-13.8	-15.5	-15.1	-15.9	-15.5 \pm 0.8	-8.9	4.1 +1.1/-1.6
534J	Paleosol carbonate nodule	100	-6.1	-14.2	-15.9	-15.5	-16.3	-15.9 \pm 0.8	-9.3	4.1 +1.1/-1.6
534K	Paleosol carbonate nodule	100	-5.5	-12.8	-14.5	-14.1	-14.9	-14.5 \pm 0.8	-7.9	3.8 +1.0/-1.5
534L	Paleosol carbonate nodule	100	-3.5	-16.7	-18.3	-17.9	-18.7	-18.3 \pm 0.8	-11.7	4.7 +1.3/-1.8
418B	Paleosol carbonate nodule	50	-7.0	-16.2	-17.9	-17.5	-18.3	-17.9 \pm 0.8	-11.3	4.6 +1.3/-1.8
418A	Paleosol carbonate nodule	49	-7.1	-16.1	-17.8	-17.4	-18.2	-17.8 \pm 0.8	-11.2	4.6 +1.3/-1.8
431L	Groundwater calcite nodule	48	-8.5	-15.6	-17.2	-16.8	-17.6	-17.2 \pm 0.8	-10.6	4.5 +1.2/-1.8
417D	Paleosol carbonate nodule	47	-10.4	-14.9	-16.6	-16.1	-17.0	-16.6 \pm 0.8	-10.0	4.3 +1.2/-1.7
431K	Groundwater calcite nodule	42	-8.9	-15.2	-16.9	-16.5	-17.3	-16.9 \pm 0.8	-10.3	4.4 +1.2/-1.7
431I	Paleosol carbonate nodule	41	-8.7	-15.9	-17.6	-17.2	-18.0	-17.6 \pm 0.8	-11.0	4.5 +1.3/-1.8
431H	Lacustrine limestone	40	-8.8	-16.0	-16.8	-15.8	-18.0	-16.9 \pm 2.2	-12.3	4.8 +1.4/-1.8
431G	Paleosol carbonate nodule	40	-7.2	-15.7	-17.4	-17.0	-17.8	-17.4 \pm 0.8	-10.8	4.5 +1.2/-1.8
417C	Paleosol carbonate nodule	39	-10.4	-12.6	-14.3	-13.9	-14.7	-14.3 \pm 0.8	-7.7	3.7 +1.0/-1.4
431F	Paleosol carbonate nodule	29	-6.6	-16.0	-17.6	-17.2	-18.1	-17.7 \pm 0.8	-11.1	4.6 +1.3/-1.8
Mean elevation (km)*										4.4 +1.3/-1.7

Note: The unique $T(\Delta_{47})$ values from clumped-isotope samples (bold) were used to calculate the calcite-water fractionation for those samples. The average $T(\Delta_{47})$ values for pedogenic and lacustrine clumped-isotope samples were used to calculate the appropriate calcite-water fractionation for the remaining samples, by sample type. VPDB—Vienna Peedee belemnite; VSMOW—Vienna standard mean ocean water.

*Error estimates for mean elevations are reported as the quadrature of the model error for each elevation estimate.

TABLE 2. STABLE-ISOTOPE DATA FOR ALL CARBONATES AND CALCULATED PALEOELEVATIONS OF THE OIYUG BASIN.

Sample	Carbonate type	Location in section (m)	$\delta^{13}\text{C}$ (‰, VPDB)	$\delta^{18}\text{O}_c$ (‰, VPDB)	$\delta^{18}\text{O}_w$ (‰, VSMOW)			Mean $\delta^{18}\text{O}_w$ $\pm 2\sigma$ (‰)	$^*\Delta(\delta^{18}\text{O}_w)$ (‰)	Model elevation (km $\pm 2\sigma$)	
Oiyug Formation (Fm.)				$T(\Delta_{47})$ ($^{\circ}\text{C} \pm 3.6$ $^{\circ}\text{C}$) [§] :			14.0 $^{\circ}\text{C}$	17.6 $^{\circ}\text{C}$	10.4 $^{\circ}\text{C}$		
				α (siderite-H ₂ O):			1.03328	1.03252	1.03413		
621I	Calcite marl	1580	1.3	-28.0	-30.1	-29.4	-30.8	-30.1 \pm 1.5	-25.5	6.5 \pm 1.8/-2.3	
621H	Calcite marl	1584	-0.1	-27.4	-29.9	-29.1	-30.7	-29.9 \pm 1.6	-25.3	6.5 \pm 1.8/-2.3	
621F	Siderite nodule	1575	12.9	-10.8	-13.1	-12.4	-14.0	-13.2 \pm 1.5	-8.6	3.6 \pm 1.1/-1.4	
								Mean elevation (km)*	6.5 \pm 1.8/-2.3		
Upper Gazhacun Fm.				$T(\Delta_{47})$ ($^{\circ}\text{C} \pm 3.6$ $^{\circ}\text{C}$) [§] :			14.0 $^{\circ}\text{C}$	17.6 $^{\circ}\text{C}$	10.4 $^{\circ}\text{C}$		
				α (siderite-H ₂ O):			1.03328	1.03252	1.03413		
618A	Siderite nodule	690	4.2	-17.1	-18.2	-17.4	-19.1	-18.3 \pm 1.7‰	-11.7	4.4 \pm 1.3/-1.8	
Middle Gazhacun Fm.				$T(\Delta_{47})$ ($^{\circ}\text{C} \pm 3.6$ $^{\circ}\text{C}$) [§] :			14.0 $^{\circ}\text{C}$	17.6 $^{\circ}\text{C}$	10.4 $^{\circ}\text{C}$		
				α (dolomite-H ₂ O)**:			1.03393	1.03312	1.03484		
				α (calcite-H ₂ O):			1.03084	1.03007	1.03169		
555	Pedogenic calcite	670	-5.8	-20.0	-21.6	-20.8	-22.6	-21.7 \pm 1.8	-15.1	5.1 \pm 1.5/-2.0	
W8	Dolomite nodule	680	-7.3	-7.6	-10.5	-9.8	-11.4	-10.6 \pm 1.6	-4.0	2.1 \pm 0.6/-0.6	
553	Calcareous shale	677	-3.8	-13.0	-11.8	-10.9	-12.7	-11.8 \pm 1.6	-5.2	3.0 \pm 0.9/-1.1	
W7	Dolomite nodule	670	-5.4	-5.5	-8.5	-7.7	-9.3	-8.5 \pm 1.7	-1.9	1.1 \pm 0.3/-0.1	
W3	Dolomite nodule	654	-6.3	-5.7	-8.7	-7.9	-9.5	-8.7 \pm 1.6	-2.1	1.2 \pm 0.4/-0.1	
W2	Dolomite nodule	649	-5.1	-5.5	-8.5	-7.7	-9.3	-8.5 \pm 1.7	-1.9	1.1 \pm 0.3/-0.1	
551	Calcareous mudstone	647	-2.5	-11.6	-11.6	-10.9	-12.4	-11.6 \pm 1.6	-5.0	2.5 \pm 0.7/-0.8	
W1	Dolomite nodule	645	-5.4	-5.8	-8.8	-8.0	-9.6	-8.8 \pm 1.6	-2.2	1.3 \pm 0.3/-0.2	
550	Dolomite nodule	615	-11.3	-11.3	-14.2	-13.5	-15.1	-14.3 \pm 1.6	-7.7	3.4 \pm 1.0/-1.3	
554B	Pedogenic calcite	570	-7.8	-19.7	-25.0	-24.2	-25.9	-25.0 \pm 1.7	-18.4	5.6 \pm 1.5/-2.1	
								Pedogenic-derived mean elevation (km)*	5.3 \pm 1.5/-2.0		
								Lacustrine-derived mean elevation (km)*	2.0 \pm 0.6/-0.7		
Lower Gazhacun Fm.				$T(\Delta_{47})$ ($^{\circ}\text{C} \pm 8.2$ $^{\circ}\text{C}$) [§] :			18.9 $^{\circ}\text{C}$	27.1 $^{\circ}\text{C}$	10.7 $^{\circ}\text{C}$		
				α (calcite-H ₂ O):			1.03279	1.03105	1.03477		
548	Pedogenic calcite	559	-8.0	-20.1	-21.5	-20.8	-22.2	-21.5 \pm 1.5	-14.9	5.0 \pm 1.4/-2.0	
165Ca	Pedogenic calcite	556	-6.9	-19.8	-18.7	-17.1	-20.5	-18.8 \pm 3.4	-12.2	4.5 \pm 1.4/-1.7	
165D	Pedogenic calcite	556	-7.1	-20.0	-18.9	-17.3	-20.7	-19.0 \pm 3.4	-12.4	4.5 \pm 1.4/-1.7	
165Fa	Pedogenic calcite	556	-6.9	-19.7	-18.6	-17.0	-20.4	-18.7 \pm 3.4	-15.0	5.0 \pm 1.5/-1.9	
165Fb	Pedogenic calcite	556	-6.8	-19.7	-18.6	-17.0	-20.4	-18.7 \pm 3.4	-15.0	5.0 \pm 1.5/-1.9	
165Fc	Pedogenic calcite	556	-5.9	-18.0	-16.9	-15.3	-18.7	-17.0 \pm 3.4	-13.3	4.7 \pm 1.5/-1.8	
165G	Pedogenic calcite	556	-6.8	-19.6	-18.5	-16.9	-20.3	-18.6 \pm 3.4	-14.9	5.0 \pm 1.5/-1.9	
R2	Pedogenic calcite	555	-7.0	-20.2	-19.1	-17.5	-20.9	-19.2 \pm 3.4	-15.5	5.1 \pm 1.5/-1.9	
547	Pedogenic calcite	540	-6.0	-19.1	-18.0	-16.4	-19.8	-18.1 \pm 3.4	-14.4	4.9 \pm 1.5/-1.8	
546	Pedogenic calcite	532	-6.4	-21.1	-20.0	-18.4	-21.8	-20.0 \pm 3.4	-16.4	5.3 \pm 1.5/-2.0	
543B	Groundwater calcite	452	-3.3	-19.5	-18.5	-16.8	-20.3	-18.5 \pm 3.4	-11.9	4.4 \pm 1.4/-1.6	
543A	Pedogenic calcite	450	-7.6	-19.4	-16.1	-15.7	-16.7	-16.2 \pm 1.0	-9.6	3.9 \pm 1.2/-1.6	
								Mean elevation (km)*	4.5 \pm 1.5/-1.7		
Rigongla Fm.				$T(\Delta_{47})$ ($^{\circ}\text{C} \pm 4.3$ $^{\circ}\text{C}$) [§] :			9.8 $^{\circ}\text{C}$	14.1 $^{\circ}\text{C}$	5.5 $^{\circ}\text{C}$		
				α (calcite-H ₂ O):			1.03180	1.03081	1.03281		
579	Pedogenic calcite	410	-6.2	-18.9	-19.8	-18.9	-20.8	-19.8	-13.2	4.7 \pm 1.4/-1.9	
576	Groundwater calcite	290	-3.4	-20.4	-21.3	-20.4	-22.3	-21.3	-14.7	5.0 \pm 1.4/-2.0	
575E	Groundwater calcite	285	-3.7	-11.9	-12.8	-11.8	-13.7	-12.8	-6.2	2.9 \pm 0.9/-1.0	
575C	Groundwater calcite	280	-2.6	-16.8	-17.7	-16.8	-18.7	-17.7	-11.1	4.3 \pm 1.3/-1.7	
575B	Groundwater calcite	278	-3.8	-13.9	-14.8	-13.9	-15.8	-14.8	-8.2	3.6 \pm 1.1/-1.3	
								Mean elevation (km)*	4.1 \pm 1.3/-1.6		
Nianbo Fm.				$T(\Delta_{47})$ ($^{\circ}\text{C} \pm 8.2$ $^{\circ}\text{C}$) [§] :			3.0 $^{\circ}\text{C}$	11.2 $^{\circ}\text{C}$	-5.2 $^{\circ}\text{C}$		
				α (calcite-H ₂ O):			1.03342	1.03147	1.03548		
W0628-3	Paleosol	44	-1.5	-24.9	-26.8	-25.0	-28.7	-26.8 \pm 3.7	-20.2	5.9 \pm 1.5/-2.1	
W0628-2	Lacustrine limestone	34	-4.1	-24.6	-27.0	-25.2	-29.0	-27.0 \pm 3.8	-20.4	5.9 \pm 1.5/-2.1	
W0628-1	Paleosol	0	-3.5	-18.6	-21.6	-21.0	-22.1	-21.6 \pm 1.1	-15.0	5.0 \pm 1.4/-2.0	
								Mean elevation (km)*	5.6 \pm 1.5/-2.1		

Note: Samples with Δ_{47} measurements are in bold. For these samples, their unique $T(\Delta_{47})$ was used to calculate $\delta^{18}\text{O}_w$. VPDB—Vienna Pee Dee belemnite; VSMOW—Vienna standard mean ocean water. Water-carbonate oxygen fractionation factors: calcite/water $\alpha = \text{EXP}[(18.03 \times 10^9/T) - 32.42/1000]$ (Kim and O'Neil, 1997); siderite/water $\alpha = \text{EXP}[(2.62 \times 10^9/T) - 2.17/1000]$ (Zhang et al., 2001); dolomite/water $\alpha = \text{EXP}[(2.73 \times 10^9/T) + 0.26/1000]$ (Vasconcelos et al., 2005).

*Error estimates for mean elevations are reported as the quadrature of the model error for each elevation estimate.

[†] $\delta^{18}\text{O}_c$ of all samples except the Nianbo Formation have been previously published in Currie et al. (2005) and Currie et al. (2016). All $\delta^{18}\text{O}_w$ values were calculated using new $T(\Delta_{47})$ measurements.

[§]Temperature error is reported as the standard error of the mean of all clumped-isotope measurements from that formation or sample type.

[¶]Low-elevation $\delta^{18}\text{O}_w$ values: -6.6‰ for Rigongla and Gazhacun Formations; -4.6‰ for Oiyug Formation, based on warm month mean temperature (WMMT) derived from Khan et al. (2014) and Siwalik Formation paleosol carbonate data (Quade and Cerling, 1995; Quade et al., 2013).

**Temperature used for dolomite-water and calcite-water fractionation factors of lacustrine samples is the average of lacustrine calcite clumped-isotope temperatures, as these would have the most similar depositional conditions.

TABLE 3. ISOTOPIC DATA FOR ALL CLUMPED-ISOTOPE SAMPLES

Sample and lithology	CO ₂ ²⁻ (wt%)	δ ¹⁸ O ₂₀₀ [*] (‰, VPDB)	δ ¹³ C [†] (‰, VPDB)	δ ¹⁸ O ₂₀₀ [†] (‰, VSMOW)	δ _{47, SG-WG} [†]	Δ _{47, GDES} ^{†,§} (‰)	T(Δ ₄₇) [#] (°C)	δ ¹⁸ O _w ^{**} (‰, VSMOW)	Number of analyses	Formation
OIYUG BASIN										
<i>Nodular and groundwater calcite</i>										
621H	36	-27.4	-0.1 ± 0.0	12.4 ± 0.1	-9.4 ± 0.1	0.698 ± 0.016	13.0 ± 3.7	-27.6 ± 1.6	11	Oiyug
W0628-1	90	-18.6	-3.3 ± 0.0	22.1 ± 0.1	-2.7 ± 0.1	0.755 ± 0.011	0.7 ± 2.3	-21.6 ± 1.1	6	Nianbo
<i>Lacustrine/marl calcite</i>										
621I	37	-28.0	1.3 ± 0.0	12.1 ± 0.0	-8.4 ± 0.0	0.689 ± 0.015	15.0 ± 3.5	-30.1 ± 1.5	12	Oiyug
W0628-2	11	-24.6	-3.3 ± 0.1	17.3 ± 0.3	-7.6 ± 0.2	0.572 ± 0.027	45.7 ± 8.3	-18.5 ± 2.9	3	Nianbo
<i>Pedogenic calcite</i>										
555	21	-20.0	-5.8 ± 0.0	19.8 ± 0.1	-7.6 ± 0.1	0.668 ± 0.017	19.7 ± 4.2	-21.7 ± 1.8	7	Middle Gazhacun
554B	51	-19.7	-7.9 ± 0.0	20.0 ± 0.1	-9.2 ± 0.1	0.739 ± 0.017	3.9 ± 3.4	-25.0 ± 1.7	4	Middle Gazhacun
548	29	-20.1	-8.4 ± 0.0	19.6 ± 0.0	-10.1 ± 0.1	0.721 ± 0.020	7.6 ± 3.3	-21.5 ± 1.5	5	Lower Gazhacun
543A	55	-19.4	-7.7 ± 0.0	21.2 ± 0.0	-8.0 ± 0.0	0.625 ± 0.010	30.1 ± 2.6	-16.2 ± 1.0	4	Lower Gazhacun
579	18	-18.9	-5.8 ± 0.2	20.9 ± 0.1	-7.0 ± 0.3	0.711 ± 0.020	9.8 ± 4.3	-19.8 ± 1.9	6	Upper Rigongla
W0628-3	6	-24.9	-1.2 ± 0.1	14.6 ± 0.3	-8.1 ± 0.2	0.738 ± 0.040	5.3 ± 8.2	-26.8 ± 3.7	3	Nianbo
<i>Vein calcite</i>										
543Av	N.D.	-27.1	-2.7 ± 0.0	14.6 ± 0.0	-9.9 ± 0.0	0.467 ± 0.014	83.3 ± 6.0	-15.1 ± 1.7	2	Lower Gazhacun
PENBO BASIN										
<i>Lacustrine/marl calcite</i>										
504A	54	-17.8	-0.7 ± 0.1	23.1 ± 0.4	0.5 ± 0.4	0.549 ± 0.003	52.4 ± 1.2	-10.5 ± 0.4	3	Nianbo
448D	42	-12.0	-4.1 ± 0.1	29.2 ± 0.3	3.4 ± 0.3	0.586 ± 0.007	40.9 ± 2.4	-6.7 ± 0.9	2	Nianbo
P0929-c	29	-12.7	-3.3 ± 0.1	28.1 ± 0.0	3.1 ± 0.0	0.701 ± 0.023	11.9 ± 5.6	-13.1 ± 2.5	2	Nianbo
DL104-3b	34	-12.4	-2.4 ± 0.1	28.4 ± 0.2	4.4 ± 0.3	0.717 ± 0.022	8.5 ± 5.0	-13.6 ± 2.2	3	Nianbo
440D	N.D.	-16.3	-3.7 ± 0.1	24.9 ± 0.1	-0.6 ± 0.1	0.540 ± 0.006	55.2 ± 1.5	-8.5 ± 0.5	2	Nianbo
<i>Pedogenic calcite</i>										
446D	54	-17.3	-3.0 ± 0.1	23.5 ± 0.1	-1.2 ± 0.1	0.557 ± 0.008	49.9 ± 2.9	-10.4 ± 1.0	3	Nianbo
440B	8	-17.2	-4.2 ± 0.1	23.7 ± 0.1	2.1 ± 0.1	0.726 ± 0.008	6.3 ± 1.8	-18.9 ± 0.8	2	Nianbo

Note: The Zaarur et al. (2013) thermometer was determined on carbonate samples digested at 25 °C and is therefore most appropriate for our analyses. Temperatures derived from our least-altered samples are in the ~1–30 °C range in the Oiyug Basin and ~6–12 °C in the Penbo Basin. VPDB—Vienna Pee Dee belemnite; VSMOW—Vienna standard mean ocean water; N.D.—no data. Italicized sample names, Δ₄₇ values, and calculated temperatures denote samples petrographically interpreted as geochemically altered or secondary calcite.

*Measured on a Delta V gas bench.

†Measured on a MAT253.

‡Carbon dioxide equilibrium scale of Dennis et al. (2011).

§Zaarur et al. (2013): T (°C) = $\sqrt{[52,600/(\Delta_{47} - 0.0520)] - 273.15}$.

**The measured oxygen-isotope composition of the carbonate and measured T(Δ₄₇) were used to calculate the oxygen-isotope value of water in equilibrium with the carbonate. As some samples are interpreted as “secondary” calcite, these water values are different than those used in the elevation calculations.

published (Currie et al., 2016; Fig. 1) and new oxygen-isotope compositions of lacustrine and pedogenic carbonates ($n = 141$) to better estimate δ¹⁸O_w of paleowaters (Tables 1 and 2). The δ¹⁸O_w value is the isotopic composition of the water from which the carbonate formed, assuming equilibrium. We used this value to represent the precipitation-weighted hypsometric mean isotopic composition of surface water, which then was entered into standard stable-isotope paleoaltimetric determinations (Rowley, 2007).

Geologic Setting

Linzizong Volcanic Arc, Southern Lhasa Block

Cretaceous–Early Tertiary Gangdese arc magmatism is commonly attributed to northward subduction of Indian oceanic lithosphere beneath Tibet (Burg et al., 1983; Tapponnier et al., 1986, 1981). Neotethyan oceanic lithosphere attached to the Indian plate was subducted beneath southern Eurasia prior to and during the early stages of continent-continent collision along the Indus-Yarlung suture—the tectonic boundary between the Indian subcontinent and Eurasia (Murphy et al., 1997; Ding and Lai, 2003). The volcanism represented by the Linzizong Group (ca. 69–43 Ma) and post-

Early Cretaceous (younger than 100 Ma) Gangdese batholiths constituted the active continental margin of southern Eurasia.

Portions of the central to northern Lhasa terrane were covered in shallow-marine platform sediments during the Aptian–Albian, potentially as far south as the Penbo Basin (Kapp et al., 2005; Leier et al., 2007), demonstrating that much of the Lhasa terrane was at sea level in the mid-Cretaceous (Zhang, 2000). These marine sequences place a lower bound on the uplift history of the southern margin of Eurasia, but the timing of the tectonic and magmatic rise of the southern Lhasa terrane and Linzizong volcanic arc to modern elevation remains controversial.

Penbo-Linzhou Basin

The Penbo, also referred to as the Linzhou, Basin (Fig. 1B) is located ~35 km north of Lhasa and 75 km north of the Indus-Yarlung suture. The modern hypsometric mean elevation of the basin drainage area is ~4200 m, with surrounding peaks <5300 m. The samples in this study were collected from modern elevations of 3950–4200 m.

This basin exposes a sedimentary and volcanic record spanning pre- to syncollisional time (ca. 67 to ca. 48 Ma) and is the type locality of the nonmarine Linzizong Group (He et al.,

2007). Here, the stratigraphic thickness of the Linzizong Group is ~3500 m (He et al., 2007). We focused our paleoelevation reconstruction in the Penbo Basin primarily on the ca. 56.5 to ca. 53 Ma Nianbo Formation and the ca. 50 Ma upper Pana Formation because they preserve abundant lacustrine limestone and groundwater and paleosol carbonate nodules, and they have pre- to early syncollisional depositional ages. The age range of the sampled Linzizong stratigraphy of the Penbo Basin is well constrained by zircon U/Pb radiometric ages of tuffs near the base and top of the measured stratigraphy (Ding et al., 2014; He et al., 2007). Additionally, a hornblende ⁴⁰Ar/³⁹Ar age from a mafic dike intruding the Nianbo Formation provides a latest possible age of Linzizong deposition within Penbo Basin (Yue and Ding, 2006).

The sedimentary rocks of the Nianbo Formation in the Oiyug Basin are mapped as age-correlative with the type Nianbo Formation in the Penbo Basin. These ages, together with stratigraphic and lithological correlation, allow us to place the paleoaltitude results from the Nianbo Formation, discussed later herein, in the Oiyug Basin into temporal and regional context.

The ~240-m-thick Paleocene–Eocene Nianbo Formation (Fig. 2) unconformably overlies the lower Upper Cretaceous Shexing Formation

Stratigraphic Log of the Nianbo Formation, Linzhou, Southern Tibet

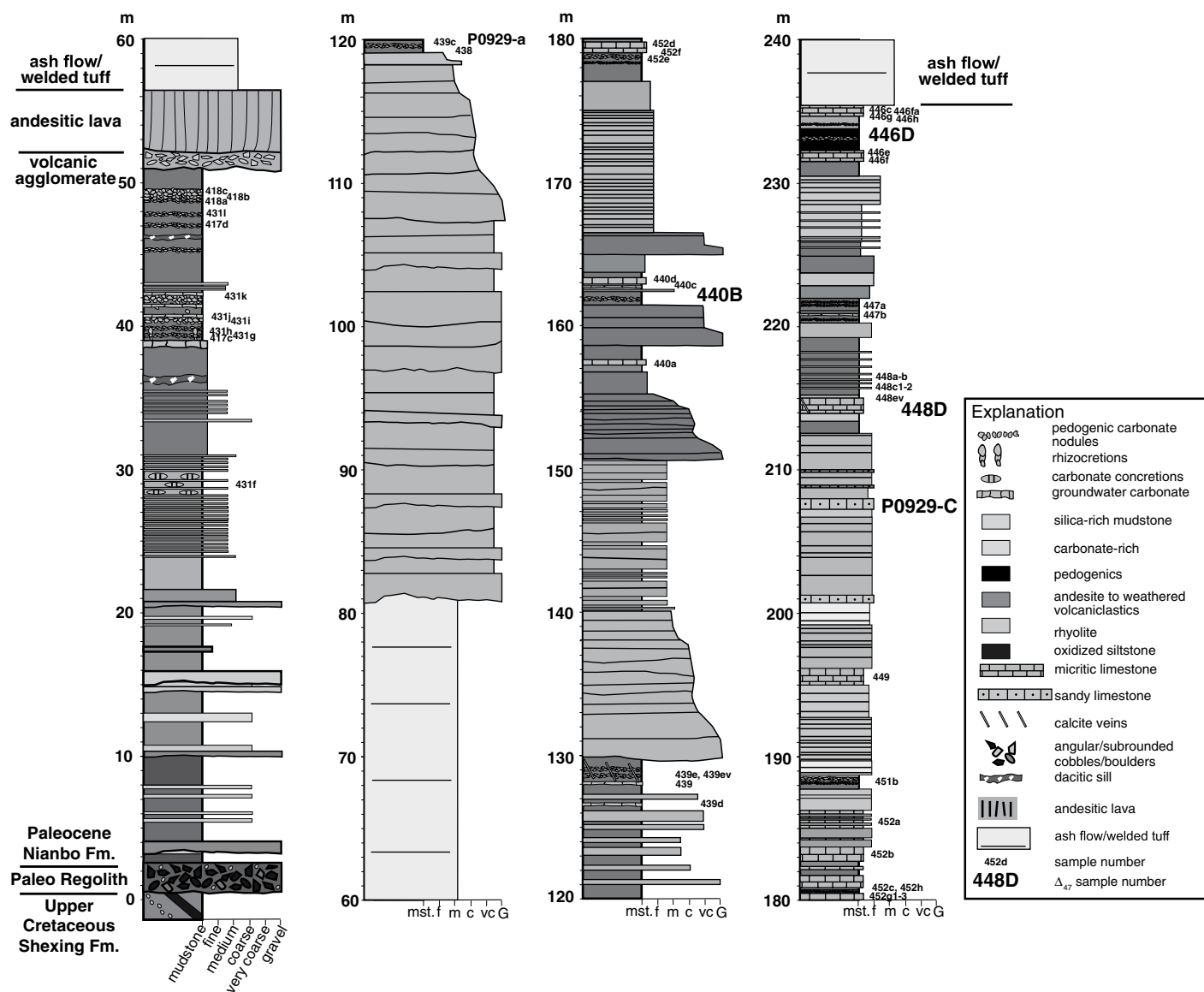


Figure 2. Composite stratigraphic section of the Nianbo Formation in the Penbo Basin. The geographic location for the base of this section is 29.999603°N, 91.209293°E. Coordinates for other measured sections within the Nianbo Formation (blue rectangles; Fig. 1B) are 29.9689°N, 91.2147°E and 29.9715°N, 91.1951°E. The base of the Pana Formation measured section is located at 30.0105°N, 91.1470°E.

in this section. Nearby, the Nianbo Formation conformably to disconformably overlies the Paleocene Dianzhong Formation, which in turn unconformably overlies the Shexing and Takena Formations. The Linzizong Group and particularly the Nianbo Formation are spatially heterogeneous, such that no section in the field is representative. Nonetheless, the overall stratigraphy and sedimentology of the Nianbo Formation can be broken into three lithologic sequences: two upward-fining packages and an ash-flow tuff and massive conglomerate between the two. The lower subunit is dominated

by purple and green laminated mudstones and volcaniclastic-dominated sandstones at its base. The mudstones contain nodular carbonate, pedogenic features, mottling, and bioturbation, and at least one nondeformed snail shell. These are overlain by fine-grained red siltstones abundant in pedogenic carbonate interbedded with yellow to brown lacustrine marls. Fossil ostracods are found in the marls. Shell morphology is preserved, but body cavities have sparry calcite infill. The uppermost part of the lower Nianbo Formation preserves well-developed calcic paleosols (Fig. 3).

The middle Nianbo subunit is defined by a period of vigorous volcanic activity. The volcanic agglomerate base is topped by a 5-m-thick andesitic lava flow. A 25-m-thick welded tuff/ash flow tops this sequence, followed by ~40 m of gravel conglomerate.

The basal 10 m of the upper Nianbo subunit is composed of interbedded red mudstones and medium to very coarse sandstones. The uppermost mudstones contain groundwater carbonate horizons and abundant pedogenic carbonate. An ~10 m section of coarse to gravel conglomerate overlies the ped-rich layers. The conglomerate is

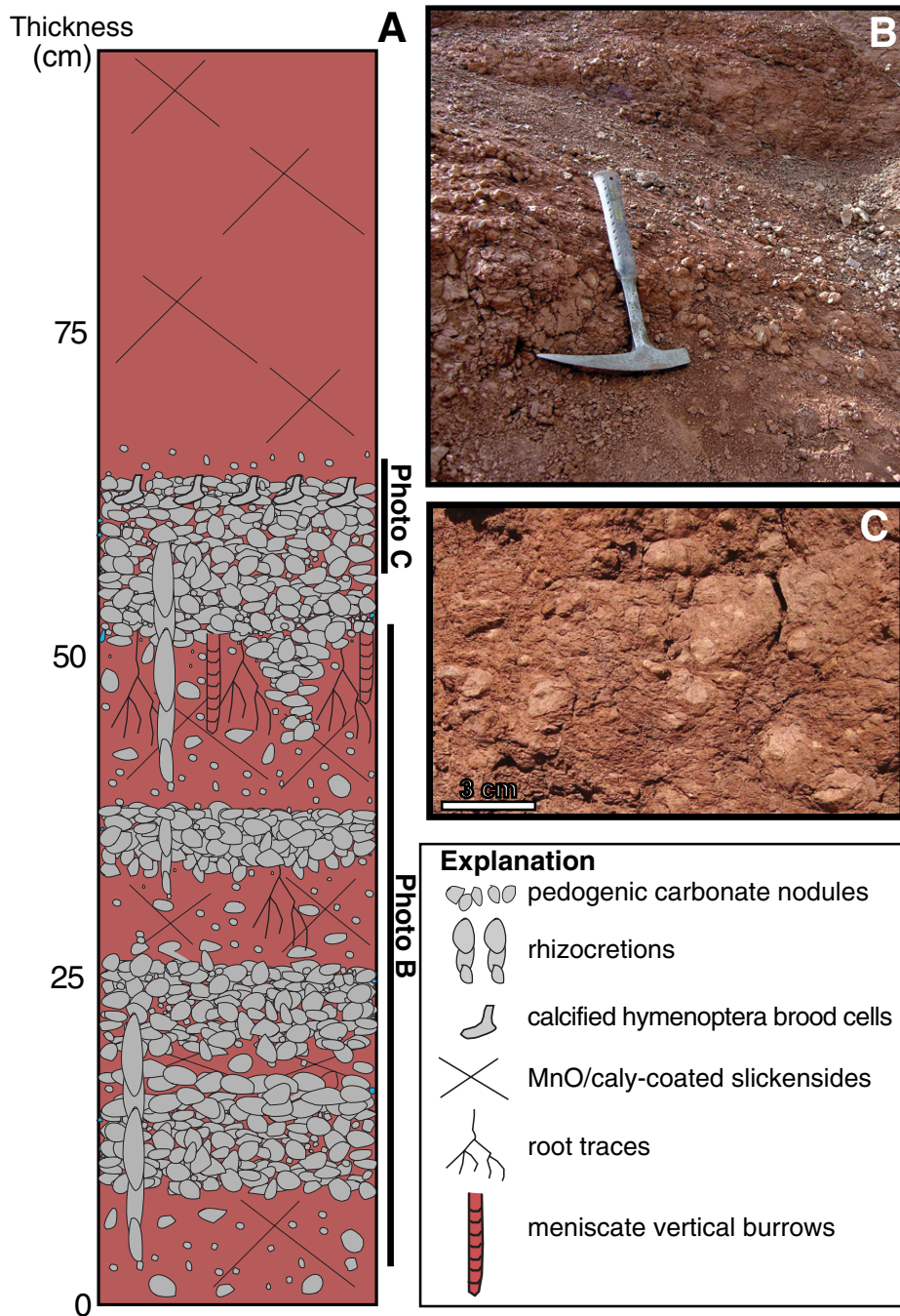


Figure 3. Example of calcic paleosols from the lower Nianbo Formation. (A) Depth profile of series of stacked paleosols developed in sandy alluvial mudstones at ~49 m in Nianbo Formation measured section (Fig. 2). Paleosols contain vertic features, root traces, insect burrows, pedogenic nodules, and rhizcretions. Paleosols are interpreted as compound in nature with four clay-rich horizons containing vertic features overlying related calcic horizons (stage III; Machette, 1985). Uppermost vertic horizon is ~1 m thick. (B) Outcrop photo of paleosol described in part A. (C) Close-up of pedogenic nodules and mudstone near the top of the upper calcic horizon described in part A.

topped by ~10 m of alternating fine and coarse sandstones. The uppermost ~80 m of the Nianbo are more variable in composition and depositional conditions, including fining-upward conglomerates, meter-thick micritic limestone beds, horizontally laminated medium-grained sandstones, sandy limestones, and paleosol horizons. Ostracods are found in one of the uppermost lacustrine limestone beds, implying a period of relatively shallow and open lakes with long residence times (Ding et al., 2014). The majority of the samples used for measuring the paleoelevation of the Nianbo Formation were derived from this upper subunit.

The uppermost preserved rocks of the Linzizong Group are the Pana Formation, a lower sequence of mostly andesitic volcanics and volcanoclastics overlain by a predominantly lacustrine succession of shales, mudstones, sandstones, and both pedogenic and lacustrine carbonates. The upper subunit of the Pana Formation was deposited between 50.5 ± 2.4 Ma and 48.4 ± 1.0 Ma, as dated by U/Pb zircon laser-ablation geochronology (Ding et al., 2014). Additionally, Eocene-age volcanic dikes cut the Nianbo and lower Pana Formations (He et al., 2007). Locally, Linzizong sediments may have experienced elevated temperatures due to this intrusive activity.

Oiyug Basin

The Oiyug Basin (Fig. 1C), also referred to as the Wuyu Basin, and mischaracterized as the Namling Basin (Spicer et al., 2003), which actually lies slightly farther west, is located 160 km west of Lhasa and 60 km north of the Indus Yarlung suture. The basin covers an area of ~300 km² (Wang and Chen, 1999) of the Lhasa terrane. Sampled localities are currently at elevations of 4300–4400 m, with surrounding elevations >5600 m. The modern hypsometric mean elevation of the basin drainage area is ~4600 m.

Paleogene–Neogene strata in the Oiyug Basin consist of the Paleocene Dianzhong Formation, the Paleocene–Eocene Nianbo Formation, the Oligocene–Miocene Rigongla Formation, the Miocene Gazhacun Group, and the Miocene–Pliocene Oiyug Formation. In this basin, the Nianbo Formation is composed of andesite, fluvial volcanoclastics, lacustrine sandstones, mudstones and limestones, and argillaceous/calcareous paleosols. In this study, an ~500-m-thick section of the Nianbo Formation was measured in the northern part of the Oiyug Basin (Fig. 4). The section is bordered to the south by a low-angle thrust fault that places Nianbo sediments above the younger Rigongla Formation. To the north, the section is separated from the overlying Rigongla Formation by an angular

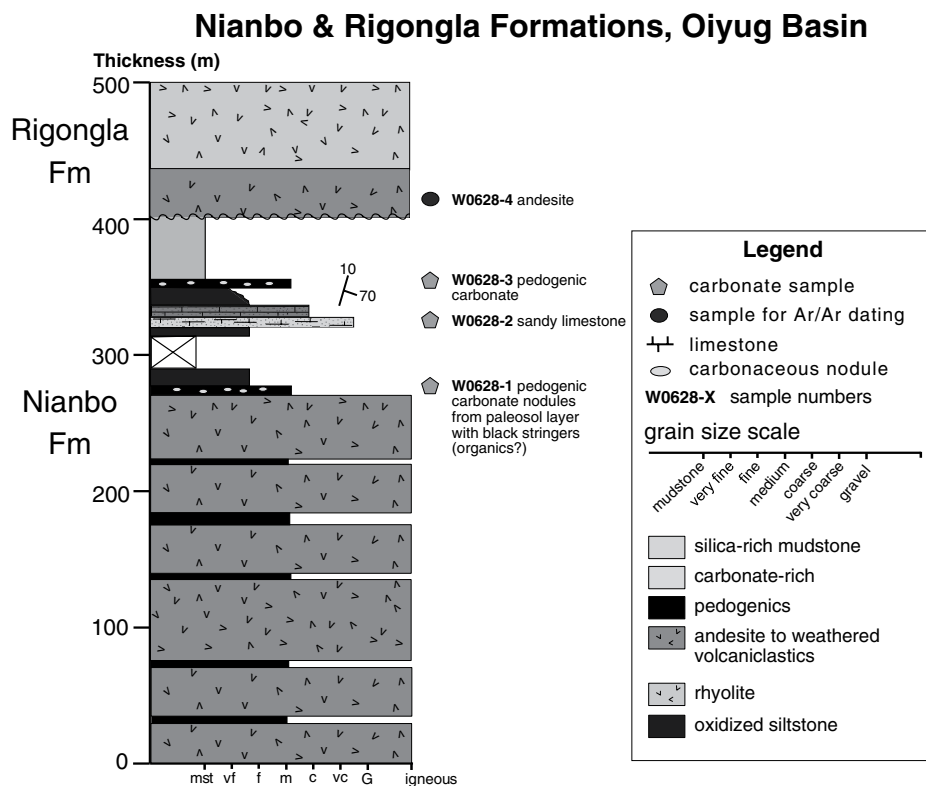


Figure 4. Stratigraphic section of the Nianbo Formation in the Oiyug Basin. The geographic location for the base of this section is 29.9594°N, 89.7414°E.

unconformity. The angular unconformity marks an erosional surface that removed upper Nianbo and Pana Formation sediments from this location prior to Rigongla Formation deposition (Fig. 1C).

The lower parts of the measured Nianbo Formation (Fig. 4) consist of ~270 m of andesitic volcaniclastic rocks sparsely interbedded with thin (~20–30-cm-thick) paleosol horizons. Pedogenic calcite (W0628-1) was collected from a moderately developed paleosol horizon ~275 m above the base of the section. Pedogenic calcite nodules in this part of the section are gray-green, texturally micritic, and typically elongate (~1 cm × 2–3 cm), surrounded by red muddy matrix. The matrix material is primarily composed of weathered volcanics.

Above the volcanics and weathered volcanics, the Nianbo Formation is dominated by lacustrine limestone, sandstone, and mudstone. The depositional environment is interpreted as marginal lacustrine. The dominant lithology at the base of the thick limestone package is laminated sandy limestone (W0628-2) with very fine-grained calcareous matrix and fine to medium quartz grains. The sandy beds interbedded with the marl limestone cliffs are interpreted as terrestrial alluvium deposited in an offshore to

nearshore lake environment (Mack and Rasmussen, 1984). The sedimentology of this sequence and environmental interpretations align with the lithology and sequence stratigraphy of the upper subunit of the Nianbo Formation in the Penbo Basin (Ding et al., 2014; this study). Approximately 10 m above this sampling locality, sandy limestone fines to oxidized siltstone and red mudstone with authigenic calcareous concretions (W0628-3). The Nianbo Formation in the Oiyug Basin is mapped as Paleocene to early Eocene in age. While undated in the immediate study area, U/Pb ages from the Nianbo Formation sampled ~40 km to the west near Namling range from 63.78 ± 0.46 Ma to 50.2 ± 2.2 Ma (Wang et al., 2014), in line with dating in the type area in the Penbo Basin to the east.

Rigongla Formation rhyolitic and andesitic volcaniclastic rocks lie unconformably above the described section of Nianbo Formation. A rhyolite (W0628-4) sampled from these volcanics yielded a late Oligocene age of 28.90 ± 1.52 Ma (K-feldspar ⁴⁰Ar/³⁹Ar; Table 4; Fig. A1 [see footnote 1]), similar to a ca. 31 Ma K/Ar age reported for the lower Rigongla Formation elsewhere in the basin (Zhu et al., 2006). Given these ages, and the ca. 50 Ma age for the upper Nianbo Formation in the region, ~20 m.y.

of rock record is likely missing at the unconformity between the Nianbo and Rigongla Formations in the study area. Additional radiometric ages of volcanics interbedded with the Linzizong strata are needed in order to assess the continuity of the rock record preserved in the Oiyug Basin.

The Rigongla Formation measured at the headwaters of the Ramaqu River consists of dacitic to andesitic volcanic rocks interbedded with an upward-fining >500-m-thick sedimentary sequence of conglomerates, sandstones, and mudstones (Fig. 1C; Currie et al., 2016). Paleosol and groundwater carbonate nodules were collected from an ~20-m-thick mudstone horizon between alluvial-fan and fluvial channel conglomerate sequences in the Rigongla Formation (Currie et al., 2016). The nodules are texturally micritic and 3–15 cm in diameter.

The Gazhacun Group, previously described as the Manxiang Formation (Zhu et al., 2006), directly overlies the volcanics of the upper Rigongla Formation. The base of the Gazhacun Group is composed of ~140 m of red and gray overbank mudstones and sparse fluvial channel sandstones and conglomerates (Currie et al., 2016). The overbank mudstones host clay-rich paleosol horizons with well-developed pedogenic calcite nodules 0.25–1.5 cm in diameter. The middle Gazhacun Group is interpreted to record a lacustrine depositional environment, represented by ~225 m of gray, green, and light-red shale and mudstone, and thin beds of siltstone and fine-grained sandstone (Currie et al., 2016). Samples from lacustrine strata of the middle Gazhacun Group are both early diagenetic calcite and dolomite nodules. Given the paucity of datable volcanics in the Rigongla Formation and lower-middle Gazhacun Group strata, the age of this stratigraphic interval is liberally bracketed between two K-feldspar ⁴⁰Ar/³⁹Ar ages from the units above and below the lower Gazhacun Group: a rhyolite in the Rigongla Formation (28.90 ± 1.52 Ma) and a felsic tuff in the upper Gazhacun Group (ca. 15 Ma; Spicer et al., 2003).

The upper Gazhacun Group, measured along the Badamaqen, consists of ~100 m of tuffaceous conglomerate and fining-upward sandstone, interbedded with carbonaceous siltstone, mudstone, shale, and coal. A siderite nodule (618A) and four shales were collected for isotopic analyses near the top of the floral locality section of Spicer et al. (2003) and Khan et al. (2014). The age of the top of the upper Gazhacun Group is constrained by a ⁴⁰Ar/³⁹Ar age of ca. 15 Ma from felsic tuff deposits within the upper part of the unit and from the base of the overlying Zongdang Group (Spicer

TABLE 4. APATITE (U-Th)/He THERMOCHRONOMETRY AND K-FELDSPAR Ar/Ar GEOCHRONOLOGY RESULTS

Aliquot*	Corrected age [†] (Ma)	F _T [‡]	²³⁸ U (nmol/g)	²³² Th (nmol/g)	¹⁴⁷ Sm (nmol/g)	⁴ He (nmol/g)	Mass (μg)	Raw age (Ma)	U (ppm)	Th (ppm)	Sm (ppm)
L0706-2 granite intrusion Penbo Basin											
X	15.10 ± 0.10	0.703	100.968 ± 0.114	200.385 ± 0.888	113.781 ± 0.109	1.992 ± 0.010	3.31	10.44	24.21	46.50	114.05
Y	16.56 ± 0.11	0.807	48.015 ± 0.072	95.882 ± 0.540	63.609 ± 0.031	1.204 ± 0.004	11.66	13.24	11.51	22.25	63.760
Z	12.93 ± 0.08	0.727	75.998 ± 0.175	345.718 ± 1.483	422.563 ± 0.201	1.875 ± 0.008	4.17	9.21	18.22	80.22	423.58
Mean age (±1σ)	14.86 ± 1.83										
L0706-3 granite intrusion Penbo Basin											
X	11.50 ± 0.06	0.793	89.580 ± 0.180	473.757 ± 2.001	738.337 ± 0.301	2.347 ± 0.007	9.44	8.98	21.48	109.93	740.11
Y	12.35 ± 0.07	0.742	179.654 ± 0.215	501.425 ± 2.131	399.745 ± 0.195	3.459 ± 0.011	4.88	9.02	43.08	116.35	400.70
Z	14.36 ± 0.09	0.717	91.660 ± 0.177	199.523 ± 0.854	150.095 ± 0.094	1.811 ± 0.008	3.78	10.14	21.98	46.30	150.46
Mean age (±1σ)	12.74 ± 1.47										
Aliquot	³⁶ Ar _a (moles)	³⁷ Ar _{ca} (moles)	³⁸ Ar _{ci} (moles)	³⁹ Ar _k (moles)	⁴⁰ Ar _r (moles)	Apparent age (Ma)	2σ error (Ma)	⁴⁰ Ar* (%)	³⁹ Ar _k (%)	K/Ca	Error (2σ)
W0628-4 Rigongla Formation Oiyug Basin											
1	6.27E-17	3.54E-15	6.52E-18	8.73E-15	7.09E-14	33.81	0.50	79.28	34.44	1.06	4.92E-0
2	1.17E-16	4.33E-15	2.61E-18	7.16E-15	6.92E-14	40.19	0.63	66.66	28.22	0.71	3.25E-0
3	8.62E-17	6.36E-15	3.56E-18	9.47E-15	8.02E-14	35.27	0.44	75.89	37.34	0.64	2.79E-0
Inverse isochron age (±2σ)	28.90 ± 1.52										

Note: (1) Isotope abundances were corrected for blank, mass discrimination, nucleogenic interferences, and postirradiation decay. (2) GA1550 flux monitor (age = 98.790 ± 0.543 Ma) was used to calculate J = 0.00169000 ± 0.00001690. (3) Error is reported at the 2σ level and includes uncertainty in J. (4) Isotope abundances were calculated with instrument sensitivity of 8.20 × 10⁻¹⁷ moles/fA.

*Single-crystal conventional (U-Th)/He analyses.

[†](U-Th)/He ages were calculated from total measured abundances in all cases, not concentrations.

[‡]Correction factor for α-ejection (Farley et al., 1996).

et al., 2003). The Zongdang Group consists of ~1900 m of ash-flow tuffs and volcanoclastics (Zhu et al., 2006; Chen et al., 2008). Ash-flow tuffs from the uppermost Zongdang Group yielded K/Ar ages ranging from 8.23 ± 0.13 Ma to 7.92 ± 0.15 Ma (Chen et al., 2008).

The Upper Miocene–Pliocene Oiyug Formation conformably to unconformably overlies the Zongdang Group. This unit is an ~1-km-thick package of basin-centered lacustrine deposits and associated basin-margin fan delta, fluvial, overbank, and swamp deposits (Zhu et al., 2006). The upper Oiyug Formation is dominated by lacustrine marl and mudstone (Currie et al., 2016). Lacustrine marl calcitic limestone, shales, nodular calcite, and nodular siderite were collected for isotopic analyses from the middle to upper Oiyug Formation, with an interpreted depositional age of ca. 5 Ma (Chen et al., 2008).

METHODS

In this study, we determined the δ¹⁸O_{carb} and δ¹³C_{carb} values of 105 carbonate samples collected from Paleocene to Eocene strata in the Penbo Basin and 36 carbonate samples from the Eocene to Pliocene strata in the Oiyug Basin. Of these samples, 7 from Penbo and 12 from Oiyug were used to determine clumped-isotope estimates of carbonate precipitation temperature T(Δ₄₇). Currie et al. (2016) reported carbon and oxygen stable-isotope compositions of Oligocene to Pliocene strata in the Oiyug Basin, and this work adds new stable-isotope compositions from Paleogene strata. We obtained a potassium feldspar total fusion ⁴⁰Ar/³⁹Ar age for Rigongla Formation volcanics in the Oiyug Basin in order

to provide an upper bound for Nianbo Formation deposition. We measured apatite (U-Th)/He ages for the Qianggeren granite in the Penbo Basin in order to constrain the erosional unroofing age.

Carbonate Sample Preparation

The outer layer of carbonate samples was removed to expose fresh material for stable-isotope analysis and to make petrographic slides. Samples were powdered using a Freedom TX low-speed drill with a Brasseler USA #2 HP round bit at low speed to avoid significant frictional heating and the potential for carbonate C-O bond reordering.

Petrographic slides were made for a subset of samples that appeared minimally altered or unaltered in hand sample in order to evaluate visual signs of aqueous alteration (dissolution features, recrystallization textures, secondary carbonates, authigenic metal oxide precipitates, etc.; see Tables 5 and 6). Petrographic analyses allow distinction between two contrasting textural relationships among preserved carbonates. One group consists of pedogenic carbonate nodules and lacustrine limestone, some of which preserve ostracods and charophyte debris within a micritic matrix with only very minor spar-filled vugs and/or microspar recrystallization (Tables 5 and 6). This minimally altered group also includes wackestones lacking evidence of secondary recrystallization. The second group, consisting of lacustrine limestone and pedogenic carbonate nodules, is characterized by varying degrees of alteration, including extensive development of sparry calcite, oxidation,

crosscutting veins, and increase in grain size of the formerly micritic matrix and sparry calcite veins. Later herein, we discuss our isotopic results with respect to our petrographic assessment of degree of alteration.

For the Penbo Basin, the Δ₄₇ analyses were carried out independently from the petrographic observations (isotopic measurements and petrographic observations were shared only after both were completed). This blind test was carried out at Miami University as a means of assessing our ability to correctly characterize alteration by petrographic observation. For the Oiyug Basin, petrographic and Δ₄₇ analyses were both completed at the University of Chicago, Chicago, Illinois.

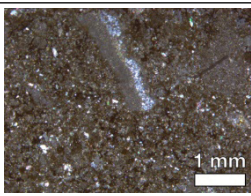
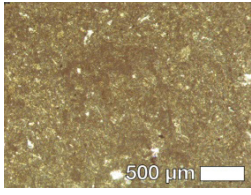
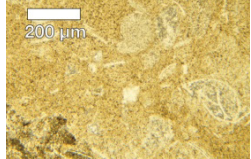
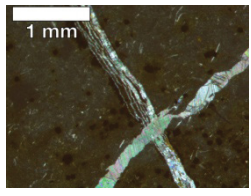
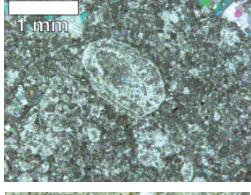
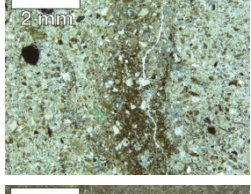
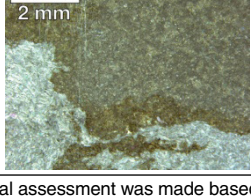
Standard Stable-Isotope Measurements

Isotopic measurements were completed in the stable-isotope facility in the Department of the Geophysical Sciences at the University of Chicago. All samples were analyzed for calcite δ¹⁸O_c and δ¹³C_c and weight percent CaCO₃ using a Gas Bench II (Thermo, Bremen, Germany) connected to a Delta V Plus (Thermo) stable-isotope ratio mass spectrometer. Stable oxygen and carbon isotopic measurements are reported in per mil (‰) using conventional delta notation, where

$$\delta^{18}\text{O}_c = \left\{ \left[\frac{(^{18}\text{O}/^{16}\text{O})_{\text{sample}}}{(^{18}\text{O}/^{16}\text{O})_{\text{standard}}} \right] - 1 \right\} \times 1000\text{‰}, \quad (2)$$

with analogous formulation for δ¹³C_c. All carbonate oxygen and carbon isotopic compositions are reported on the VPDB scale.

TABLE 5. PETROGRAPHY OF PENBO BASIN CARBONATES

Sample	Petrographic image	Textural description	Petrographic interpretation	T(Δ_{47}) (°C)
446D		Abundant sparry calcite filling voids and veins; silicification	Diagenetic/high T	49.9 ± 2.9
DL104-3b		Microspar and small amount of dense micrite; recrystallized ostracods; minor vuggy calcite spar	Primary/low T	8.5 ± 5.0
P0929-c		Microspar with patchy dense micrite; sparry vuggy calcite; some silicification	Primary/low T	11.9 ± 5.6
448D		Dense micrite to microspar; ostracods; vein calcite and pyrite	Diagenetic/high T	40.9 ± 2.4
440D		Microspar/sparry calcite; silicification; ostracod fossils	Minor alteration	55.2 ± 1.5
440C		Sparry calcite; calcite veins; silicification	Diagenetic/high T	–
446H		Coarse microspar/sparry calcite; fibrous calcite	Diagenetic/high T	–

Note: An initial assessment was made based on presence or absence of alteration textures. T(Δ_{47}) values are included for the samples that were analyzed for Δ_{47} .

(±0.1‰ analytical uncertainty). The calculated values for water in isotopic equilibrium with the carbonate minerals, $\delta^{18}O_w$, are reported on the VSMOW scale.

Clumped-Isotope (Δ_{47}) Analyses

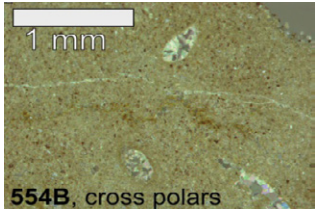
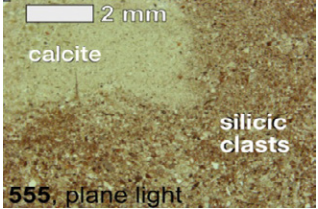
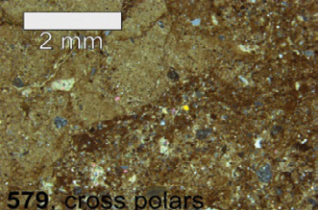
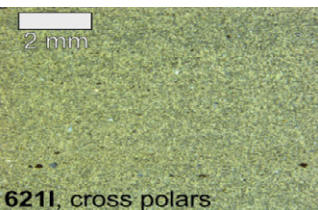
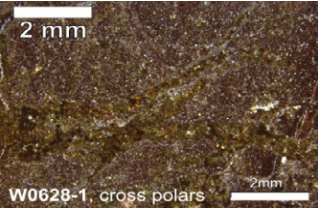
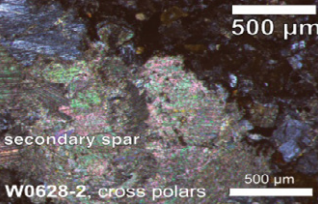
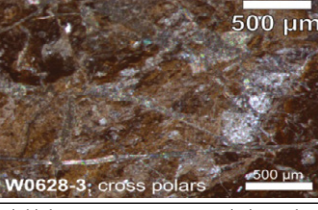
The carbonate clumped-isotope thermometer was established using the temperature-dependent enrichment of “clumped” isotopologues in carbonates, and it can be used to determine carbonate mineralization temperature (e.g., Ghosh et al., 2006a, 2006b; Eiler, 2007; Huntington et al., 2009). The “clumping” refers to ions or molecules with more than one rare isotope (e.g., a clumped carbonate ion: $^{13}C^{18}O^{16}O_2^{2-}$). The formation of carbonate minerals in internal isotopic equilibrium results in greater clumping at lower temperatures. The clumped-isotope composition of carbonates is measured on CO_2 released by phosphoric acid digestion of carbonate minerals. The composition is reported as a Δ_{47} value expressed in units of per mil (‰), where Δ_{47} is defined as the enrichment in clumped CO_2 with molecular mass 47 (dominated by $^{13}C^{18}O^{16}O$) relative to the amount of clumping expected based on a stochastic distribution of C and O isotopes as measured in the bulk isotopic composition: $\Delta_{47} = (R^{47}/R^{47*} - 1) \times 1000‰$, where $R^{47} = \text{mass } 47/\text{mass } 44$, and R^{47*} denotes analogy to R^{47} but reflects the abundance predicted with a random distribution of isotopes. The value δ_{47} is defined similarly to $\delta^{13}C$ and $\delta^{18}O$, using the abundance ratios of CO_2 isotopologues (rare mass 47 isotopologues compared to the common mass 44 isotopologue) referenced to a working gas that defines “zero.”

Carbonates were digested overnight in 5–7 mL of ~103% anhydrous phosphoric acid at 26 °C with acid densities of 1.92–1.94 g/cm³, verified gravimetrically prior to each use. Following acid digestion, the resultant CO_2 was purified on a glass vacuum line to remove trace water vapor and isobaric contaminants. Gas was transferred through a cryogenic water trap (glass tubing immersed in LN₂-ethanol slurry at –80 °C) with the CO_2 frozen out (LN₂) downstream and with noncondensable gases then pumped away. These noncondensable gases typically gave a pressure of 0.1–0.2 Torr in a 250 mL volume segment of the vacuum line and reaction vessel, as compared with a CO_2 partial pressure of 80 Torr in 15 mL. The frozen CO_2 sample was isolated from the rest of the system and warmed, with pressure reading serving as a monitor of CO_2 yield from the sample digestion (902 piezo vacuum transducer, MKS Instruments, Andover, Massachusetts). Then, the CO_2 was passed through a U-trap (6 mm inner diameter, 24 cm packed length) filled with

Samples were weighed out to yield roughly 100–200 μg $CaCO_3$ equivalent. Comparable size ranges of the isotopic standards NBS-18 ($\delta^{13}C = -5.01‰$ VPDB; $\delta^{18}O = -23.20‰$ VPDB; Coplen et al., 2006), NBS-19 ($\delta^{13}C = 1.95‰$ VPDB; $\delta^{18}O = -2.19‰$ VPDB; Gonfi-

antini, 1983), and periodically LSVEC ($\delta^{13}C = -46.6‰$ VPDB; Coplen et al., 2006) were interspersed with the Tibetan samples. These standards were used to assess, and correct for when needed, linearity and drift. Results for carbonate $\delta^{13}C_c$ and $\delta^{18}O_c$ are reported on the VPDB scale

TABLE 6. PETROGRAPHY OF OIYUG BASIN CARBONATES

Sample	Petrographic image	Textural description	Petrographic interpretation	$T(\Delta_{47})$ (°C)
554B		Matrix-supported limestone; very fine-grained micritic matrix; numerous microfossils <1 mm	Primary/low T	3.9 ± 3.4
555		Red-brown matrix with gray, micritic, centimeter-sized regions (labeled); no visible recrystallization or iron rims between calcite and oxidized siliciclastics	Primary/low T	19.7 ± 4.2
579		Fissures traverse the slide from left to right (likely micron-scale veins); abundant ~1 mm rounded quartz crystals (sand clasts); mud matrix; hematite rim on micritic region?	Minor alteration	9.8 ± 4.3
6211		Slightly recrystallized sparry calcite matrix mixed with micrite; finely laminated	Primary/low T	15.0 ± 3.5
W0628-1		Clast-supported and loosely lithified birefringent vein with an iron-stained rim of a different texture	Primary/low T	0.7 ± 2.3
W0628-2		Clast-supported; extensive crosscutting of veins; pervasive infill of sparry calcite in fissures	Diagenetic/high T	45.7 ± 8.3
W0628-3		Matrix appears to have been micritic but has been extensively crosscut by sparry veins	Diagenetic/high T	5.3 ± 8.2

Note: An initial assessment was made based on presence or absence of alteration textures. $T(\Delta_{47})$ values are included.

Haysep Q (60/80 mesh, Supelco, Bellefonte, Pennsylvania), with an ~2-cm-thick layer of powdered Ag_3PO_4 (Strem Chemicals, Newburyport, Massachusetts) mixed with quartz chips at the inlet end. Small quartz wool plugs capped with silver wool plugs were used on both ends of the column to retain fine mesh and powder packing material. The U-trap thus packed served as a chromatography column. We optimized the temperature of CO_2 chromatography by varying temperature of the column from 0 to 25 °C and passing gases equilibrated at 25 °C and 1000 °C through the column. No fractionation of the equilibrated gases occurred during the room temperature trials. The transfer of CO_2 through the column at room temperature was monitored barometrically, and freezing over of CO_2 was continued for ~10 min beyond the time required for the upstream pressure to reach baseline (40–45 min total). The collected CO_2 was cryogenically transferred through a second water trap to a cold finger and then isolated and warmed for pressure reading to confirm quantitative transfer. The purified CO_2 was stored in borosilicate tubes with chlorotrifluoroethylene (CTFE) valve body and O-ring seal (Kimble-Chase, Vineland, New Jersey) until loaded into the mass spectrometer sample bellows.

Clumped-isotope measurements and traditional carbon and oxygen stable-isotope measurements were made on a Finnigan MAT253 set to measure m/z 44–49 ion beams. We employed the run structure and pressure baseline correction detailed in He et al. (2012). Oztech (Safford, Arizona) isotopic standard CO_2 tank gas (UOC 1766, $\delta^{13}C = -3.61\text{‰}$ VPDB, $\delta^{18}O = 24.99\text{‰}$ VSMOW) was used as the working reference gas during clumped-isotope analyses, and δ_{47} values were determined with the working gas defining zero.

Following Dennis et al. (2011), raw Δ_{47} values were standardized to gases heated to 1000 °C to approximate near-random distribution of isotopes, as well as gases equilibrated with waters of known composition at 4 °C, 26 °C, and 60 °C. Standardized Δ_{47} values are reported on an “absolute reference frame,” henceforth referred to as the carbon dioxide equilibrium scale (CDES) following Dennis et al. (2011) and allowing for interlaboratory comparison. We routinely measured standard calcite materials (Carrera Marble [CM] and four $CaCO_3$ materials from ETH-Zurich [ETH1 through 4]), which are analyzed at regular intervals in many clumped-isotope facilities for the purpose of interlaboratory calibrations and measurement comparisons. We also used frequent analyses of these standard materials as a check on internal consistency of repeated measurements within and between analytical periods (Tables A1 and A2 [see footnote

1]). Further discussion of quality-control checks and corrections applied to measurements made on the MAT253 can be found in the Appendix (see footnote 1).

Temperatures were calculated using the Zaarur et al. (2013) paleothermometer. There is presently a consensus in the clumped-isotope research community that the conversion of Δ_{47} values to equilibrium temperatures should employ a paleothermometer that was determined on similar sample types and with similar acid digestion temperatures (Huntington et al., 2015; Deffliese et al., 2015; Gallagher and Sheldon, 2016; Burgener et al., 2016; Ringham et al., 2016). Our 26 °C acid digestion temperature is essentially the same as the 25 °C temperature used for the Zaarur et al. (2013) calibration. Use of this paleothermometer also maintains interlaboratory consistency with other paleoaltimetry studies on the Tibetan Plateau (Huntington et al., 2015). Errors are reported for each sample using the standard error of the mean for replicate sample digestions (in this study, Δ_{47} standard error of the mean, s.e.m. of 0.011–0.040), which converts to temperature uncertainties of 2.3–8.2 °C on the Zaarur et al. (2013) paleothermometer.

⁴⁰Ar/³⁹Ar Geochronology

Standard K-feldspar ⁴⁰Ar/³⁹Ar total fusion analyses were conducted for sample W0628-4 at the Lehigh University Noble Gas Laboratory, Bethlehem, Pennsylvania (Table 4). Approximately 2.4 mg aliquots of K-feldspar were loaded into an aluminum foil packet and stacked vertically with other unknowns along with GA1550 biotite flux monitor (age = 98.79 Ma) and K₂SO₄ and CaF₂ salts to correct for nucleogenic interferences. Following a cumulative 25 h irradiation at the U.S. Geological Survey Triga reactor, K-feldspars were split into three aliquots, loaded into a sample planchette, and brought to vacuum by a turbomolecular pump coupled with a rotary backing pump. Samples were fused using a Merchantek dual ultraviolet/CO₂ laser system. Extracted gas was purified with an SAES (Milan, Italy) getter for 10 min. The gas was then measured by an Argus VI magnetic sector mass spectrometer equipped with five faraday cups. Masses 40, 39, 38, 37, and 36 were measured concurrently to enable calculation of the radiogenic ⁴⁰Ar component and to correct for nucleogenic interferences (⁴⁰Ca, ⁴²Ca, ³⁷Cl, ⁴⁰K) on Ar isotopes. Raw data were reduced using ArArCalc software (Koppers, 2002) to regress to time-zero beams and to correct for blank, mass discrimination, nucleogenic interferences, and decay following irradiation. Data for the three aliquots in the inverse isochron plot show a well-fit linear correlation

with a ⁴⁰Ar/³⁶Ar intercept indicative of a trapped excess Ar component (Fig. A1 [see footnote 1]).

Apatite (U-Th)/He Thermochronometry

Measurements for apatite (U-Th)/He thermochronometry were made at the Noble Gas Thermochronometry Laboratory at the Berkeley Geochronology Center, Berkeley, California. A brief description of the methodology is provided here; for a full description of the measurement procedures, see Tremblay et al. (2015).

Individual, euhedral apatite crystals with no visible fluid or mineral inclusions and equivalent spherical radii of 50 μm or greater were selected, photographed, and measured using a Leica MZ16 stereomicroscope. Individual crystals were loaded into PtIr packets and heated under vacuum to 1050 ± 50 °C for 6 min with an 810-nm-wavelength diode laser. The extracted gas was spiked with an aliquot of ³He, purified, and analyzed using a Pfeiffer (Asslar, Germany) Prisma quadrupole mass spectrometer QMS 200 under static vacuum. Helium blanks, determined by heating empty PtIr packets, were typically less than 5 × 10⁻¹⁷ moles. To achieve complete helium extraction, each sample was reheated until the ⁴He yield was less than 0.5% of the ⁴He yield in the first heating step. Molar ⁴He abundances were calculated by dividing the measured ⁴He/³He ratio by the ⁴He/³He ratio of a manometrically calibrated ⁴He standard gas aliquot spiked with the same molar abundance of ³He as was the unknown, and multiplying this value by the standard gas's known ⁴He molar abundance.

After degassing, each sample was dissolved in 50 μL of 7 N HNO₃ spike solution containing 9.20 × 10⁻¹⁰ mol/L ²³³U, 9.03 × 10⁻¹⁰ mol/L ²²⁹Th, and 6.7% enriched ¹⁴⁷Sm spike. Solutions were diluted by a factor of 20 and analyzed on a Thermo Scientific Neptune Plus multicollector inductively coupled plasma-mass spectrometer (ICP-MS) with an Aridus2 desolvating nebulizer sample introduction system. To standardize the analyses, we also analyzed a spiked normal solution with known U, Th, and Sm concentrations. Spiked normal solution isotope ratio measurements were reproducible to much better than 0.5% for each element. (U-Th)/He ages were calculated using blank-corrected ⁴He, ¹⁴⁷Sm, ²³²Th, and ²³⁸U abundances. Raw ages were corrected for alpha ejection effects after Farley et al. (1996).

DISCUSSION OF RESULTS

Geochronology and Thermochronometry

A rhyolite immediately above the Rigongla-Nianbo unconformity provides a ⁴⁰Ar/³⁹Ar K-

feldspar age of 28.90 ± 1.52 Ma (Fig. A1 [see footnote 1]), providing a minimum age for the underlying Nianbo Formation. A three-point regression in the inverse isochron is not ideal for these data, and xenocrystic contamination cannot be ruled out in the Rigongla rhyolite. However, if this were the case, a well-defined regression line with reasonable trapped ³⁶Ar/⁴⁰Ar intercept would require fortuitous trade-offs between each aliquot's age, trapped ³⁶Ar/⁴⁰Ar, and trapped to radiogenic Ar ratio, and therefore is not likely. The inverse isochron age of 28.9 ± 1.52 Ma that we report is consistent with a K/Ar age of ca. 31 Ma from the lower Rigongla Formation elsewhere in the basin (Zhu et al., 2006), which lends additional confidence to our interpretation.

Apatite grains from two samples of Qianggeren granite (L0706-2 and L0706-3) from a quarry ~4 km north of the Pana Formation in Penbo Basin yielded (U-Th)/He ages of 14.86 ± 1.83 Ma and 12.74 ± 1.47 Ma (1σ; Table 4), respectively. The Qianggeren granite sits in the hanging wall of the Gulu thrust. L0706-2 and L0706-3 are located <1–2 km from a reported zircon U/Pb age of 51.9 ± 2.5 Ma within the Qianggeren granite (He et al., 2007).

δ¹³C, δ¹⁸O, and Clumped-Isotope-Derived Temperatures

Penbo Basin

The oxygen-isotope compositions of all 68 calcites sampled from the Pana and Nianbo Formations in the Penbo Basin ranged from δ¹⁸O of -22.8‰ to -9.4‰ ± 0.1‰, with mean values of -14.0‰ ± 1.2‰ and -15.1‰ ± 2.1‰ (1σ), respectively (Table 1). The carbon-isotope compositions ranged from δ¹³C of -10.4‰ to -0.1‰. The mean δ¹³C_{cc} for all calcites of the Pana and Nianbo Formations varied by 1.5‰, with values of -6.0‰ ± 1.5‰ and -4.5‰ ± 2.3‰ (1σ), respectively. Pedogenic and lacustrine carbonate typically derive their carbon from different sources and precipitate under different environmental conditions, thus providing additional information for environmental reconstructions. As such, it is worth noting isotopic variability between modes of carbonate genesis. The mean δ¹³C_{cc} values for paleosol carbonate in the Paleocene–Eocene Pana and Nianbo Formations are -6.9‰ ± 0.8‰ and -5.4‰ ± 2.2‰, respectively. The mean δ¹³C_{cc} values for lacustrine carbonate are -5.7‰ ± 1.8‰ and -3.2‰ ± 1.7‰.

In the subset of samples with clumped-isotope measurements and petrographic characterization, both the “primary” carbonates and those with more extensive signs of recrystallization spanned -12‰ to -18‰ in δ¹⁸O_c space.

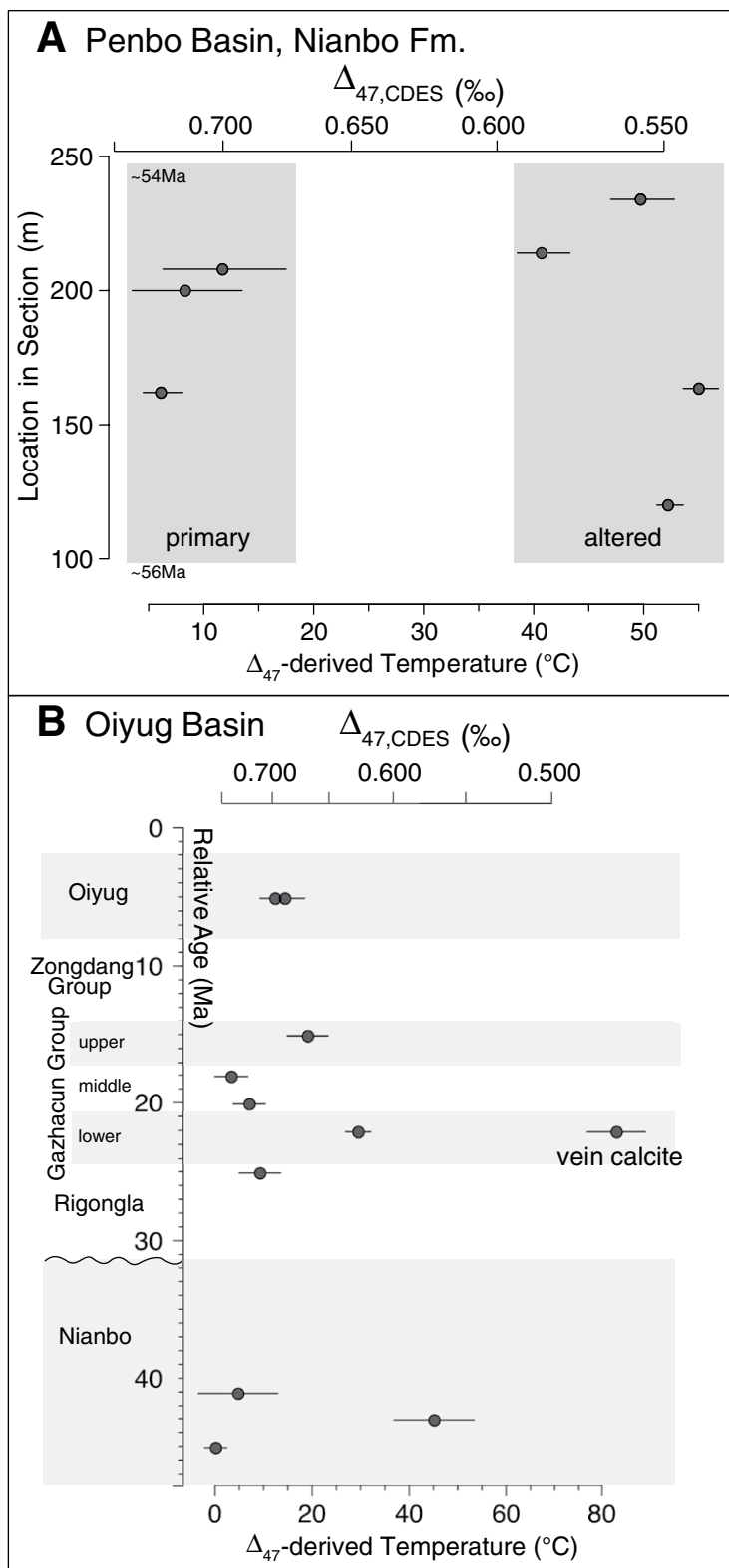


Figure 5. Clumped-isotope-derived paleotemperatures of (A) samples from the Penbo Basin with relative age, and (B) samples from the Oiyug Basin. Ages are based on location in stratigraphic section and interbedded ashes. Δ_{47} is reported in carbon dioxide equilibrium scale (CDES) reference frame (Dennis et al., 2011). Error bars represent $\pm 1\sigma$ of all replicate analyses of each sample (n listed in Table 1).

The three primary carbonates from the Nianbo Formation recorded $\Delta_{47,CDES}$ values of $0.700\text{‰} - 0.730\text{‰} \pm 0.020\text{‰}$ (Table 3). These carbonates yielded $T(\Delta_{47})$ of 6–12 °C (Fig. 5A). As described in the Methods section (Sample Preparation), we interpret these as “primary” carbonate reflecting original depositional temperature. Four pedogenic and lacustrine carbonates exhibited more extensive recrystallization in thin section. These altered carbonates have $\Delta_{47,CDES}$ values of $0.540\text{‰} - 0.590\text{‰} \pm 0.010\text{‰}$, with corresponding paleotemperatures from 41 °C to 55 °C. The upper end of this temperature range is similar to those determined from visual thermal alteration index values for organics sampled from the base of the Penbo section. These values correspond to vitrinite reflectance values (R0) of 0.4% to 0.5%, indicating burial temperatures ranging from 53 °C to 75 °C (Barker, 1988).

The observed variability in both $\delta^{18}\text{O}_c$ and Δ_{47} does not display any stratigraphic trend that can be attributed to progressive burial diagenesis with depth (Fig. 6). The samples that show petrographic and Δ_{47} signs of alteration are not appreciably shifted in $\delta^{18}\text{O}_c$, implying that the alteration in these samples was rock-buffered; i.e., carbonate buffered the oxygen-isotope composition relative to the small amount of water present in the system. We emphasize paleo-elevations derived from samples with Δ_{47} analyses (Table 3), but we included data from all samples (measured $\delta^{18}\text{O}_c$ only) under the assumption that any alteration took place in a rock-buffered system. The remainder of the discussion of the Penbo Basin samples will focus on the implications of the isotopic compositions of the minimally altered, micritic carbonates.

Oiyug Basin

Traditional oxygen- and carbon-isotope variations were assessed for trends with location in section (relative age) and sediment type (Table 2). Oxygen analyses of siderites and dolomites from the Oiyug Basin yielded different values from the dominant calcite mineralogy. For example, calcites from the Oiyug Formation (ca. 8.1–2.5 Ma; Chen et al., 2008) yielded $\delta^{18}\text{O}_c$ and $\delta^{13}\text{C}$ values of -28.0‰ to $-27.4\text{‰} \pm 0.1\text{‰}$ and $-0.1\text{‰} - 1.3\text{‰}$ (VPDB), and the siderite nodule yielded -10.8‰ and 12.9‰ . As such, siderites and dolomites are considered separately.

Calcites from the Gazhacun Group (>15.03 Ma; Spicer et al., 2003) yielded mean $\delta^{18}\text{O}_{cc}$ and $\delta^{13}\text{C}_{cc}$ values of $-18.8\text{‰} \pm 2.6\text{‰}$ (ranging -21.1‰ to -11.6‰) and $-6.3\text{‰} \pm 1.6\text{‰}$ (ranging -8.0‰ to -2.5‰). Dolomites from the Gazhacun Group yielded mean $\delta^{18}\text{O}_{MgCO_3}$ and $\delta^{13}\text{C}_{MgCO_3}$ values of $-6.9\text{‰} \pm 2.3\text{‰}$ (ranging -11.3‰ to -5.5‰) and $-6.8\text{‰} \pm 2.4\text{‰}$

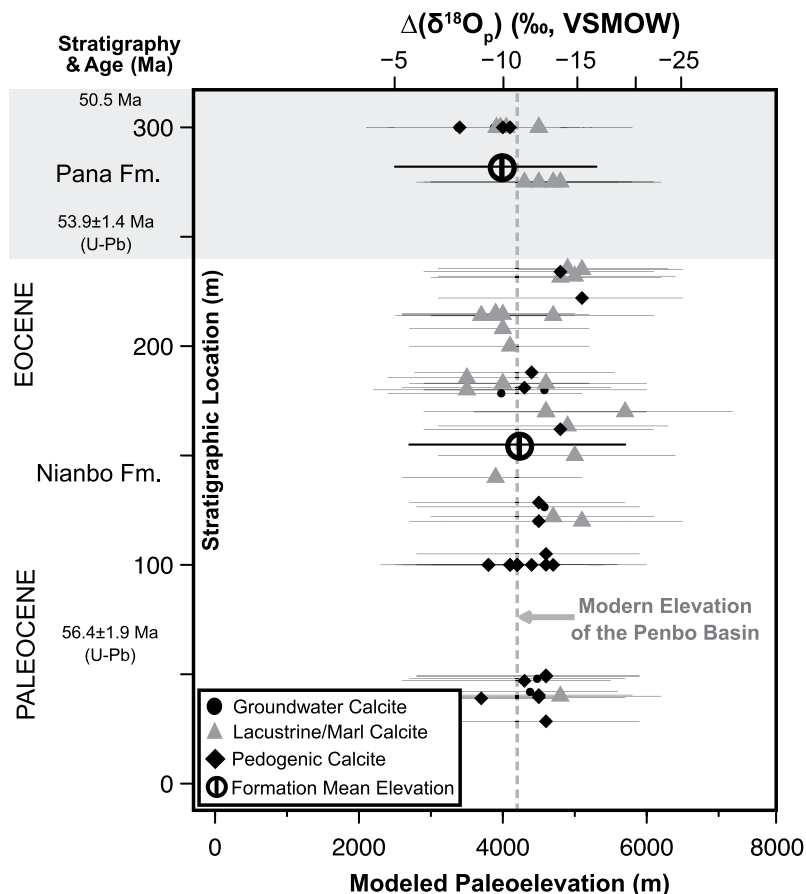


Figure 6. Paleocene–Eocene elevation reconstruction of the Penbo Basin. We used a modified version of Rowley’s (2007) paleoaltimetry model. The average of the “primary” Δ_{47} -derived temperatures for lacustrine and pedogenic carbonate was used for the $\delta^{18}O_c$ to $\delta^{18}O_w$ fractionation factors for carbonates of like lithology. Symbols are indicative of lithology. Error bars represent propagation of analytical (standard error of the mean, s.e.m.) and model error in quadrature. The mean elevation for each formation is indicated by the black circle with vertical line. The vertical dashed line marks the modern hypsometric mean elevation of the Penbo Basin.

(ranging -11.3‰ to -5.1‰). One lacustrine siderite from the top of the Gazhacun Group yielded $\delta^{18}O_{FeCO_3}$ and $\delta^{13}C_{FeCO_3}$ values of -17.1‰ and 4.2‰ , respectively. The mean $\delta^{18}O_c$ and $\delta^{13}C_{cc}$ values of calcite in the Rigongla Formation (31.4–15.1 Ma; Zhu et al., 2006) are $-16.4\text{‰} \pm 4.0\text{‰}$ (ranging -20.4‰ to -11.9‰) and $-3.9\text{‰} \pm 1.4\text{‰}$ (ranging -6.2‰ to -2.6‰), respectively. Calcites from the Nianbo Formation (63.8–50.2 Ma; Wang et al., 2014) yielded slightly lower $\delta^{18}O_c$ of -24.9‰ to $-18.6\text{‰} \pm 0.1\text{‰}$. The mean $\delta^{13}C_{cc}$ value of the Nianbo Formation was $-3.0\text{‰} \pm 1.4\text{‰}$, which agrees within error with the carbon-isotope values of the Nianbo Formation in the Penbo Basin.

Eight of the pedogenic, groundwater, and lacustrine calcites yielded $\Delta_{47,CDES}$ measurements ranging from 0.625‰ to 0.755‰ (Table 3).

These values correlate to temperatures that range from $\sim 30\text{ °C}$ to 1 °C (Fig. 5B), which are in the realm of plausible low-latitude, high-elevation surface temperatures (Lawrimore et al., 2011).

A vein calcite (543Av) from the Lower Gazhacun Formation yielded a low Δ_{47} value of $0.467\text{‰} \pm 0.014\text{‰}$ and corresponding higher temperature of $83.3 \pm 6.0\text{ °C}$ (\pm s.e.m., $n = 2$). This vein was subsampled from pedogenic calcite 543A, which yielded a Δ_{47} value of $0.625\text{‰} \pm 0.010\text{‰}$ and paleotemperature of $30.1 \pm 2.6\text{ °C}$ (\pm s.e.m., $n = 4$). Even if this pedogenic calcite precipitated at the warmest part of the day during the warmest month of the year, 30 °C is likely warm for $>4\text{ km}$ elevation. There are at least two plausible scenarios that would result in a soil carbonate $T(\Delta_{47})$ greater than mean air temperature:

(1) Pedogenic $T(\Delta_{47})$, on average, exceeds mean summer air temperature by $3\text{--}5\text{ °C}$ (Hough et al., 2014) and mean annual air temperature by $10\text{--}15\text{ °C}$ due to summertime bias in soil carbonate formation (Quade et al., 2013) and increased solar heating of the soil surface (Passey et al., 2010). Applying the latter offset, the air temperature above the location of soil carbonate formation would be $15\text{--}20\text{ °C}$. While seasonality may have the dominant effect on soil carbonate Δ_{47} (Passey et al., 2010; Suarez et al., 2011; Peters et al., 2013; Quade et al., 2013; Hough et al., 2014), Δ_{47} also varies with soil depth and duration of shade cover (Quade et al., 2013), soil moisture as it relates to the timing of carbonate formation (Burgener et al., 2016), and local soil hydrology (Ringham et al., 2016). This is to say, at the same elevation and atmospheric temperature, but under variable environmental conditions, two pedogenic calcites could record significantly different Δ_{47} values. For example, the two pedogenic calcites most proximal to 543A, within the Gazhacun Formation and 40 m below in the Rigongla Formation, yielded $T(\Delta_{47})$ values of $7.6 \pm 3.3\text{ °C}$ and $9.8 \pm 4.3\text{ °C}$, respectively. Therefore, it is reasonable to believe that the air temperature above soil carbonate 543A was much cooler than 30 °C .

(2) The bulk rock could have experienced low-grade alteration and partial recrystallization under higher temperature associated with the calcite vein (543Av). Even so, there are significant differences between $\delta^{18}O_c$ and Δ_{47} values of 543A and 543Av, suggesting that the alteration was not pervasive enough to cause extensive bond reordering or bulk isotopic resetting of the whole rock.

Marl calcite W0628-2 of the Nianbo Formation is also interpreted as diagenetically altered based on a Δ_{47} value of $0.572\text{‰} \pm 0.027\text{‰}$ (\pm s.e.m., $n = 3$) and corresponding paleotemperature of $45.7 \pm 8.3\text{ °C}$. However, the other two samples from the Nianbo Formation yielded paleotemperatures of $0.7 \pm 2.3\text{ °C}$ ($n = 6$) and $5.3 \pm 8.2\text{ °C}$ ($n = 3$; Table 3; Fig. 5B). Further, samples W0628-2 and W0628-3 were identical in $\delta^{18}O_w$ within uncertainty, regardless of the high apparent $T(\Delta_{47})$ retained by W0628-2. This suggests that the isotopic composition of the Nianbo Formation in the Oiyug Basin also reflects a rock-buffered system. As such, samples collected from this section likely have maintained oxygen-isotope fidelity even under higher diagenetic temperatures.

Multiple-Proxy Assessment of Diagenesis and Maximum Carbonate Temperatures

At sufficiently high temperature, solid-state bond reordering can occur in the carbonate lattice without the aid of water. Carbonate that

experiences temperatures >100 °C for 10^6 – 10^8 yr is subject to reordering of ^{13}C – ^{18}O bonds to a more stochastic distribution, or a lower Δ_{47} (Henkes et al., 2014). A high degree of ^{13}C – ^{18}O clumping preserved in the carbonate lattice is thought to be diagnostic of primary carbonate because no known mechanisms are currently described to alter a carbonate to a higher Δ_{47} value. However, recent measurements of latest Paleocene marine carbonates (Jialazi Formation) buried to at least 150 – 180 °C (Orme, 2015) strongly suggest that ^{13}C – ^{18}O bonds in the carbonate lattice can increase in relative abundance (increasing Δ_{47}) during burial- and exhumation-related alteration (Ingalls, 2017). The mechanism by which bond ordering can increase during alteration has yet to be adequately modeled and attributed to a geological process during burial and exhumation. Therefore, it is exceedingly important to provide multiple assessments of alteration and isotopic resetting/reordering when interpreting clumped-isotope and traditional stable-isotope data and apply caution in interpreting high Δ_{47} measurements.

The detection of diagenetic alteration and isotopic resetting requires careful characterization of carbonate mineralogy, inspection for recrystallization and alteration textures using petrography and microscopy, and subsampling of $\delta^{18}\text{O}_c$ of clasts, veins, and matrix material (DeCelles et al., 2007; Saylor et al., 2009) to detect possible diagenesis and isotopic resetting. Unfortunately, micron-scale recrystallization in the matrix and on mineral edges may go unnoticed using only these techniques (Garzzone et al., 2004; Leier et al., 2009). We therefore complemented petrographic observations with further geochemical analyses to constrain thermal history and therefore the potential for solid-state alteration.

The Oiyug and Penbo Basins are structurally complex, with major thrust faults (i.e., Gulu, Puxiabaga, and Lega thrusts; He et al., 2007) that place Mesozoic strata structurally above our Paleocene–Eocene sections. Here, we carefully consider the thermal conditions experienced by Linzizong carbonates in order to assess the significance of our stable-isotope paleoaltimetry and carbonate clumped-isotope results in the Oiyug and Penbo Basins. Constraints on the timing of Gulu thrust activation and consequent burial of the Paleocene–Eocene Linzizong strata in the Penbo Basin are limited to K-feldspar $^{40}\text{Ar}/^{39}\text{Ar}$ (He et al., 2007) and apatite (U-Th)/He thermochronometry (AHe) of the Qianggeren granite ~ 3 km north of Penbo Basin (Fig. 1). These data suggest activation of the Gulu thrust occurred after the youngest Pana Formation sedimentation (ca. 47 Ma) and prior to the exhumation of the Qianggeren granite to ~ 70 °C (<3 km depth) ca. 15–12 Ma

(AHe). The AHe ages closely match others to the east (Tremblay et al., 2015) and in the greater Lhasa region (Rohrmann et al., 2012), which are thought to reflect a period of regional exhumation of the southeastern Lhasa terrane. It is likely that the Paleocene–Eocene Linzizong strata were exhumed to <3 km depth (cooler than threshold temperature for solid-state reordering) as well during this regional exhumation event. Regional exhumation at ca. 15–12 Ma places a critical bound on Linzizong burial duration.

It is possible that the AHe ages presented here represent rock uplift associated with thrust exhumation, but multidiffusion domain modeling of K-feldspar from the Qianggeren granite yielded a thermal history that indicates rapid cooling from ~ 325 °C to <150 °C between ca. 42 and 39 Ma (He et al., 2007). We suggest that the rapid exhumation of the Qianggeren granite in the hanging wall of the Gulu thrust records the initiation of thrusting, and thus places a maximum bound on the timing of burial of the Linzizong strata.

To determine the maximum burial temperature experienced by the Linzizong sediments, we must consider contributions to the thickness of rock overburden. The absence of strata younger than the Pana Formation in the Penbo Basin and the absence of the Pana Formation at the Nianbo-Rigongla unconformity in the Oiyug Basin could both be tied to regional upper-crustal shortening (Rohrmann et al., 2012) and possibly Gulu thrust activation. It is possible that the Oligocene to Miocene strata overlying the Linzizong Group never existed in the Penbo Basin. If so, the Paleocene–Eocene Linzizong strata would have experienced thrust burial with a total overburden thickness equal to the structural thickness of the already deformed Jurassic–Triassic units. The Jurassic–Triassic units have an outcrop width of ~ 3 km north of Penbo Basin. The hanging wall of the next structural panel to the north contains the Qianggeren pluton intrusive into Linzizong strata that unconformably overlies mapped Carboniferous units (NGAC, 2002, map H45C002003). Interestingly, a Paleocene–Eocene E_1 granitoid intrudes across the Gulu thrust ~ 22.5 km farther east (29.9634°N , 91.4221°E ; NGAC, 2012, map H46C003001), implying most Gulu-associated deformation might have been related to widespread pre-Linzizong deformation of the Shexing and older units below the Maqu unconformity. Reactivation of at least a segment of the Gulu thrust post-Pana deposition is clear, but this may not have been associated with significant overthrusting of the Penbo Basin. The multiple episodes of shortening, both pre-Linzizong and post-Linzizong deposition preclude detailed

structural reconstruction of the tectonic burial history of this region.

Organic geochemical proxies, however, support a cooler thermal history for the Linzizong strata. Vitrinite reflectance from a Nianbo Formation shale (645A) in the Penbo Basin suggests these strata reached temperatures in excess of 110 °C. Preliminary methylphenanthrenes (biomarkers) derived from this shale yield equivalent vitrinite reflectance values of $1.4\% \pm 0.4\%$, suggesting that these strata reached temperatures in excess of 135 °C at some point in their burial history, but not significantly greater based on the lack of typical petroleum biomarkers (i.e., sterane and hopane) and long-chain *n*-alkanes indicative of deep burial. Assuming a very conservative 25 °C/km geothermal gradient for this arc region, these temperatures suggest no more than 6 km of total post-Nianbo burial by Pana Formation sediments and structurally emplaced overburden.

Using the kinetic parameters of Henkes et al. (2014), we can model the amount of solid-state reordering of C–O bonds within the calcite lattice that would occur under hypothetical time-temperature histories. Burial of the Nianbo strata by Pana Formation sediments plus thrust emplacement of Mesozoic rocks could contribute up to 6 km of overburden. Given the loose constraints on thrust activation and duration of burial, we model the Paleocene–Eocene strata burial to <150 °C (~ 6 km burial upon Gulu thrust activation) at ca. 42–39 Ma based on K-feldspar multidiffusion domain modeling (He et al., 2007), followed by rapid regional exhumation to below 70 °C at ca. 12 Ma (AHe; this study). Although rapid exhumation is not required by the AHe data, this scenario represents the longest possible burial duration consistent with the thermochronometric constraints. Under this scenario, we expect a Δ_{47} value of $\sim 0.590\%$, or $T(\Delta_{47})$ of 65 °C. None of the carbonates from the Penbo Basin yielded Δ_{47} values as low as this scenario, or temperatures as high.

Thus, the $T(\Delta_{47})$ measurements from the Nianbo Formation within the Penbo Basin do not appear to reflect solid-state reordering and are interpreted to record primary isotopic compositions or early recrystallization temperatures during water-rock alteration at shallow depths. There could be minimal reordering at the lower-bound temperatures from the organic thermal maturation estimates, perhaps boosting $T(\Delta_{47})$ estimates on the order of 10 °C (Stolper and Eiler, 2015). If primary temperatures were cooler than those we estimated directly, then this would result in higher paleoaltimetry estimates. We did not make any correction for this potential slight reordering, and so our altimetric estimates remain conservative. More importantly, the C–O

bonds of Nianbo Formation carbonate yielding “low” $T(\Delta_{47})$ measurements appear to be robust to elevated burial temperature no matter the precise time-temperature history of the Gulu thrust, and they are interpreted to record primary mineral formation temperatures from the Paleocene to Eocene. These samples provide apparent evidence for the survival of primary clumped-isotope values even in the face of substantial burial and heating.

Testing the Predictive Capability of Petrographic Observations in Assessing Carbonate Diagenesis

A subset of nodular, groundwater, lacustrine marl, pedogenic, and vein calcite samples from Penbo and Oiyug was selected for Δ_{47} analyses based on sedimentary and petrographic textures seen in thin section (Tables 5 and 6) in order to (1) sufficiently sample primary isotopic compositions to derive paleotemperatures of each time slice throughout the Cenozoic, and (2) provide a comparison between microscopic assessment of primary carbonate textures and direct measurements of $T(\Delta_{47})$. This enabled a check on our ability to correctly assess diagenetic alteration in thin section. Based on visual observations in petrographic section, each sample was binned as “primary” (lacking evidence of recrystallization), “minor alteration” (heterogeneous, macroscopic, and could be potentially avoided by careful sample drilling), or “diagenetic” (extensive recrystallization present).

Temperatures derived from clumped-isotope measurements generally corresponded with the petrographic interpretations for six of the seven Oiyug Basin samples. One sample, W0628-3 from the Nianbo Formation, was predicted to be diagenetic and yield a high $T(\Delta_{47})$ (low Δ_{47}) because of extensive crosscutting of secondary calcite veins. Contrary to this assessment, triplicate measurements of micrite from this sample yielded a $T(\Delta_{47})$ of 5.3 ± 8.2 °C (s.e.m.). This combination of petrographic observation and isotopic measurement suggests two possible interactions: (1) Alteration occurred very early in the rock’s history while the rock was at high elevation prior to burial, so the altered carbonate still yields a cool signal, or (2) most of the sample mass is unaltered micrite. In the second scenario, even if the calcitic veins experienced warm temperatures, they did not significantly shift the bulk Δ_{47} values. Thermochronometric data, petrography, and the Δ_{47} -derived temperatures ($T[\Delta_{47}]$) are in agreement that sediments and paleosols from the Oiyug and Penbo Basins have not reached high enough burial temperatures that would likely alter the original Δ_{47} composition of carbonates via solid-state alteration. Therefore, we consider our low $T(\Delta_{47})$ car-

bonates from both sedimentary basins to represent primary depositional conditions throughout the Cenozoic.

Paleocene to Pliocene Stable-Isotope Paleoaltimetry of the Lhasa Terrane

Penbo Basin

All clumped-isotope samples from the Penbo Basin were derived from the Nianbo Formation. As such, we used the average of the three Δ_{47} -derived “primary” paleotemperatures (8.9 ± 5.0 °C) coupled with measured $\delta^{18}\text{O}_c$ to calculate the isotopic composition of the water with which calcite equilibrated (Kim and O’Neil, 1997). Paleowater $\delta^{18}\text{O}_w$ values of the Nianbo Formation (ranging -11.8‰ to -22.6‰ VSMOW) were used to estimate elevation ($\Delta[\delta^{18}\text{O}_p]$). We report both individual elevation estimates and the mean elevation of each dominant lithology within a geologic formation (Table 1; Fig. 6).

The best estimate of the paleoelevation of the Nianbo Formation preserved in the Penbo Basin is $4.4 +1.3/-1.7$ km, comparable to modern elevation of this basin (Table 1; Fig. 6). We view this estimate to be conservative because we employed the modern isotopic lapse rate, which is likely significantly steeper than the true lapse rate in the early Eocene (Rowley, 2007; Rowley and Garzione, 2007). Further, the Siwalik value for low-latitude ($\sim 19.6 \pm 3.9^\circ\text{N}$; Quade et al., 1989), low-elevation precipitation likely has lower $\delta^{18}\text{O}$ than actual precipitation in the source region for moisture advecting to higher altitudes during the considerably warmer early Eocene. The use of an isotopically more negative low-elevation precipitation source contributes to making our paleoelevation calculations conservative, i.e., underestimates the true elevation.

We applied the mean $T(\Delta_{47})$ derived from the underlying Nianbo Formation to calculate $\delta^{18}\text{O}_w$ of the overlying upper Pana Formation sediments. This succession yielded paleosurface water isotopic compositions of -16.9‰ to -13.4‰ VSMOW. These paleoprecipitation values correspond to an estimated paleoelevation of the Pana Formation of $4.1 +1.2/-1.6$ km, identical to the underlying Nianbo Formation within error.

Oiyug Basin

The Nianbo, Rigongla, and Lower Gazhacun Formations are dominated by a common lithology (pedogenic calcite), which allows for a straightforward characterization of the Paleocene to Miocene elevation history (Table 2). For samples with clumped-isotope measurements, the sample-specific $T(\Delta_{47})$ was applied to calculate carbonate-water isotopic fractionation. An

average $T(\Delta_{47})$ value for each geologic formation was applied for samples from which only $\delta^{18}\text{O}_c$ was measured. Employing $T(\Delta_{47})$ values of 3.0 ± 8.2 °C for the Nianbo Formation, 9.8 ± 4.3 °C for the Rigongla Formation, and 18.9 ± 8.2 °C for the Lower Gazhacun member, we calculated $\Delta(\delta^{18}\text{O}_p)$ of $-18.5\text{‰} \pm 3.1\text{‰}$, $-10.7\text{‰} \pm 3.5\text{‰}$, and $-13.8\text{‰} \pm 1.9\text{‰}$ VSMOW (1σ), respectively. Taking the average ($\pm 2\sigma$ model and analytical error) of all carbonates within these formations yielded mean elevation estimates of $5.6 +1.5/-2.1$ km, $4.1 +1.3/-1.6$ km, and $4.5 +1.5/-1.7$ km, respectively (Fig. 7). The elevation estimate for the Paleocene–Eocene Nianbo Formation suggests that the Oiyug region was $0.5\text{--}1.5$ km higher at the onset of India-Asia collision than it is today.

Early and middle Miocene Gazhacun carbonate oxygen compositions spanned a broad range, -5.5‰ to -21.1‰ VPDB. All marl and lacustrine calcite, mudstones, and dolomite deposited in the middle member of the Gazhacun Group were ^{18}O -enriched relative to other units. The higher $\delta^{18}\text{O}_c$ values in the middle Gazhacun member are interpreted as the result of evaporative enrichment because pedogenic calcites from stratigraphically proximal horizons yielded low $T(\Delta_{47})$ values of $3.9\text{--}19.7$ °C with low $\delta^{18}\text{O}$ values.

Evaporative enrichment was not clearly evident in lacustrine calcite and siderite in the older Nianbo Formation or the younger Oiyug Formation. The mean elevation derived from the two calcite clumped-isotope samples in the Oiyug Formation is $6.5 +1.8/-2.3$ km, using an average $\Delta\delta^{18}\text{O}_p$ of $-24.2\text{‰} \pm 1.5\text{‰}$ (Table 2). As a comparison, the elevation estimate of siderite nodule 618A from the upper Gazhacun is $4.4 +1.3/-1.8$ km ($\Delta[\delta^{18}\text{O}_p]$ of -11.7‰). We accept the elevations provided by the calcites in the Gazhacun and Oiyug Formations because of the preservation of primary Δ_{47} values (Fig. 5B) and the evaporative trend demonstrated by plotting $\delta^{18}\text{O}$ of the two siderite samples relative to $\delta\text{D}_{\text{leaf wax}}$ and $\delta^{18}\text{O}_{\text{calcite}}$ from the same sedimentary horizon (see discussion and Fig. A2 [see footnote 1]).

Comparing Isotopic and Temperature Lapse Rates

There can be a correlation between degree of depletion of oxygen in meteoric water and formation temperature because both are controlled by atmospheric lapse rates. Estimates of tropical sea-surface temperature for times bracketing the age of the Nianbo Formation imply $T > 30$ °C (Pearson et al., 2001) and thus a temperature gradient from sea level to the Penbo Basin of $\geq 20 \pm 5$ °C. A typical 6 °C/km atmospheric lapse rate implies elevations in excess of 3 km.

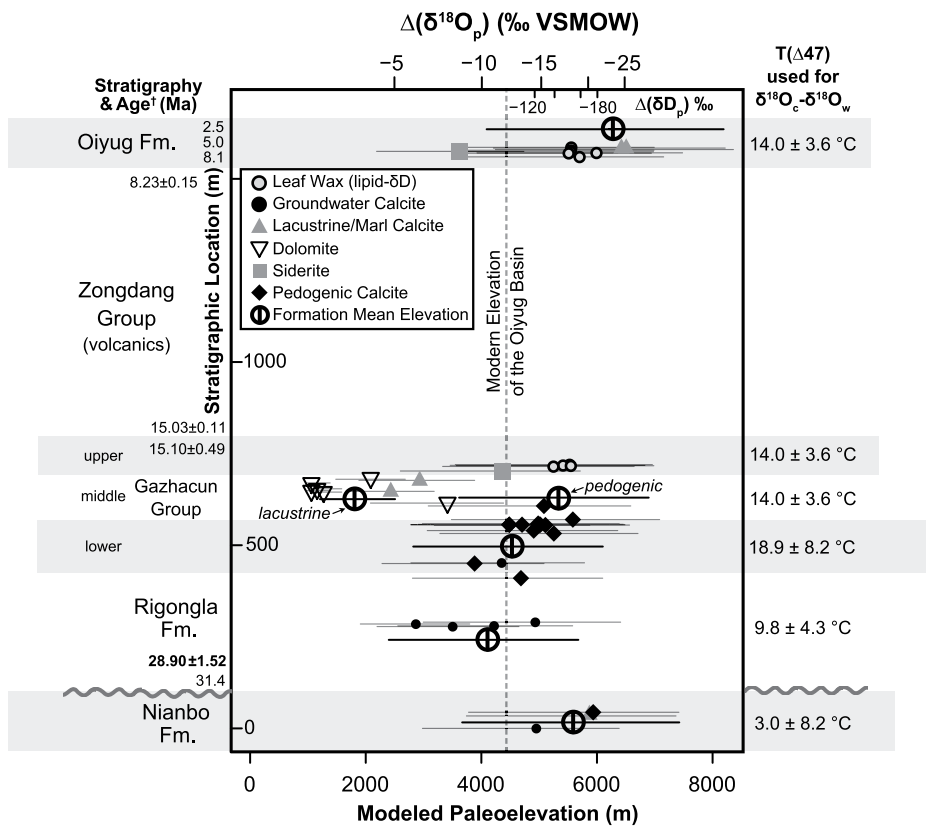


Figure 7. Cenozoic elevation reconstruction of the Oiyug Basin, southern Tibet. Calculated paleoelevations and oxygen-isotope compositions of pedogenic, lacustrine/marl, and groundwater calcite, and nodular siderite and dolomite are plotted relative to sample location in stratigraphic section and age. Symbols are indicative of lithology. Ages were taken from paleomagnetic (Chen et al., 2008) and radiometric data (Zhou et al., 2010), as well as one $^{40}\text{Ar}/^{39}\text{Ar}$ age from this study. Error bars represent propagation of analytical (standard error of the mean, s.e.m.) and model error in quadrature. The mean elevation for each formation is indicated by the black circle with vertical line. The mean elevations derived from lacustrine and pedogenic calcites in the Gazhacun Formation are plotted separately to visualize the isotopic enrichment of lacustrine dolomites and calcites. The vertical dashed line marks the modern hypsometric mean elevation of the Oiyug Basin.

Ground surface temperatures are typically warmer than the atmosphere at the same height, and pedogenic and lake carbonates appear to record this with a summer seasonal bias (Huntington et al., 2010). Thus, our paleotemperatures are also consistent with an elevation of ~4 km.

HIGH-ELEVATION SOUTHERN MARGIN OF EURASIA

Using $T(\Delta_{47})$ and $\delta^{18}\text{O}$ values of pedogenic and lacustrine carbonates from the Paleocene–Eocene Nianbo Formation, we are able to advance the elevation record of the southern Lhasa block an additional ~20 m.y. compared with the oldest prior records (Currie et al., 2016). Our oldest paleoelevations support a preexisting “high” topography on the southern margin of Eurasia

prior to the onset of India-Asia collision (Ding et al., 2014), with elevations potentially ~1 km higher than today in some areas. However, the sediments of the Nianbo Formation could have been deposited at an even higher altitude. The Paleocene–Eocene elevation estimate presented here is conservative because the isotopic lapse rate model was constructed using global mean T and RH data for the modern low-latitude ocean surface. The warmer temperatures of the Eocene would shift the $\Delta(\delta^{18}\text{O})$ -elevation relationship to higher elevation for a given offset in precipitation isotopic compositions. We accept the modern calibration as a conservative representation of past environmental conditions because we are data limited in our knowledge of the frequency distribution of low-latitude ocean surface T and RH in the Paleocene–Eocene.

The Paleocene–Eocene Nianbo Formation sits unconformably below the Rigongla Formation in the Oiyug Basin, so the elevation history between the two units is unconstrained. However, the similarity of estimated $T(\Delta_{47})$ and $\delta^{18}\text{O}$ values between the Nianbo and Rigongla units implies little variability during this interval. The Rigongla and lower Gazhacun Formations yielded elevation estimates close to the modern mean elevation of the Oiyug Basin.

A face value assessment of model elevations from the middle and upper Gazhacun Formations, when interpreted based on $\Delta(\delta^{18}\text{O}_p)$ alone, would suggest that the southern Lhasa block experienced an interval of topographic deflation to 2.5 km in the early to mid-Miocene. However, it is unlikely that the hypsometric mean elevation of the Oiyug Basin experienced subsidence from 4.5 km to 2.5 km in the Miocene, followed by an uplift to >6 km in the Pliocene, and subsidence to ~4.6 km by present day. It is more likely that the enriched oxygen values of the Gazhacun Formation are an evaporative overprint of the original precipitation signal.

However, the potential low in Miocene elevation temporally corresponds with the formation of the Kailas Basin (26–18 Ma; DeCelles et al., 2011) and the Liuqu conglomerate (ca. 21–17 Ma; Leary et al., 2017), both interpreted to have formed during an elevation low within the suture zone. The Kailas Formation, named after its type locality at Mount Kailas, extends ~1400 km along strike and is <1–4 km thick where exposed. The Kailas Basin is interpreted as a continental rift basin resulting from <5–10 km horizontal extension, attributed to rollback of the subducting Indian slab beneath Tibet (DeCelles et al., 2011). The shearing and subsequent breakoff of the Indian slab would have caused a southward and downward pull on the overlying Indian continent, resulting in enough extension to drive the subsidence necessary to form the Kailas Basin in southern Tibet (DeCelles et al., 2011). The $\delta^{13}\text{C}$ values from carbonate nodules within the Liuqu conglomerate have been used in a paleoenvironmental assessment suggesting that the Indus-Yarlung suture was wet and well-vegetated during deposition (Leary et al., 2017). These conditions are suggestive of low elevation.

Additionally, Ding et al. (2017) presented paleoenthalpy-based paleoaltimetry that agrees with a low-elevation Indus-Yarlung suture during Liuqu deposition, although they dated the deposition of Liuqu flora to the latest Paleocene (ca. 56 Ma). Ding et al. (2017) also presented paleoflora-based paleoaltimetry results from the Qiuwu Formation in Qiabulin (ca. 26–19 Ma), which more closely correlates with

the elevation estimates of Leary et al. (2017). Based on the Qiuwu Formation paleoenthalpy estimates, the Indus-Yarlung suture was already well above sea level ($\sim 2.3 \pm 0.9$ km) by this interval of the Miocene. Due to the temporal overlap of the extension associated with the formation of the Kailas Basin and Liuqu conglomerate, assuming Miocene deposition, and the deposition of the ^{18}O -enriched sediments of the middle Gazhacun member in the Oiyug Basin, it is conceivable but unlikely that the marl calcites and dolomites in this study preserve a primary isotopic signature representative of mid-Miocene precipitation at low elevation.

Further work to the west along the southern Lhasa block could determine whether the apparent lower elevations are actually a local evaporative overprint as interpreted here or are seen in the coeval carbonate record in the southern Lhasa block, and whether there is evidence elsewhere of ~ 6 km elevations at this time in the Miocene.

Past Models of the Regional Tectonic History of the Lhasa Block

The tectonic development of Earth's quintessential active continent-continent collision zone has been extensively studied for the past three decades, with particular attention paid to the development and persistence of extreme high elevations. However, the majority of previous work on the uplift history has invoked models of en masse (England and Houseman, 1986; Harrison et al., 1992; Molnar et al., 1993; Harrison et al., 1995) or local (Wang et al., 2006) plateau uplift in the Neogene. The paleoaltimetry work presented in this paper provides geochemical evidence that counters models involving late Cenozoic uplift.

Late Cretaceous to Early Cenozoic

Contrary to earlier models of Neogene uplift, Kapp et al. (2007) presented tectonic evidence that the Lhasa block must have undergone extensive crustal thickening by the early Paleogene, if not in the Cretaceous. Kapp et al. (2007) used kinematic models to demonstrate that a precollisional northward-vergent retroarc thrust belt could have accommodated >250 km of N-S shortening. They attributed an additional >160 km of shortening to the emplacement of the Lhasa-Damxung thrust sheet, which was associated with a magmatic flare-up ca. 69 Ma due to removal of thickened mantle lithosphere. Kapp et al. (2007) coined their tectonic evolution model for the Lhasa terrane the "Lhasaplano"—a Cretaceous–Early Tertiary Cordilleran-style (contractional) orogen associated with the Gangdese

magmatic arc. Our >4 km Paleocene–Eocene elevation reconstruction largely agrees with the Lhasaplano model.

Late Cenozoic

Harrison et al. (1992) and Molnar et al. (1993) asserted that the southern Tibetan Plateau reached its maximum elevation by 8 ± 1 Ma. Harrison et al. (1992, 1995) suggested that the initiation of slip on the Nyainqentanghla detachment fault was result of the Tibetan Plateau attaining its maximum potential crustal thickness for the lithospheric temperature distribution and convergence rate. They reason that slip on the NE-SW–striking Yangbajian graben northwest of Lhasa and other N-S–striking rifts are indicative of extensional orogenic collapse due to overthickening of the continental crust during shortening. K-feldspar and biotite $^{40}\text{Ar}/^{39}\text{Ar}$ thermochronological data from the uplifted footwall of the graben-defining Nyainqentanghla detachment fault are indicative of fault and shear zone initiation at 8 ± 1 Ma. Harrison et al. (1992, 1995) used the numerically modeled temperature history and slip rate (3 mm/yr) to predict that the southern Tibetan Plateau reached its elevation and crustal thickness threshold at this time and collapsed under its overthickened crustal mass by way of graben formation.

However, as has been argued previously by Currie et al. (2005, 2016), and fully consistent with the new data presented here from the Oiyug Basin, existing paleoaltimetry data from various regions of the Lhasa block, including the Nima Basin (DeCelles et al., 2007; Huntington et al., 2015), Lunpola Basin (Polissar et al., 2009; Rowley and Currie, 2006), and Himalayas (Garzzone et al., 2000; Rowley and Garzzone, 2007; Gébelin et al., 2013; Rowley et al., 2003), as well as eastern Tibet (Hoke et al., 2014; Li et al., 2015), are all consistent with little or no change in elevation in the past 20 or more million years, and thus these data are incompatible with the significant late Neogene uplift compatible with the models of Harrison et al. (1992) and Molnar et al. (1993).

IMPACT OF EVAPORATIVE ENRICHMENT OF SURFACE WATERS ON PALEOELEVATION ESTIMATES

Elevations derived from two siderite samples (621F and 618A of the Oiyug Basin) are apparently offset by up to 2 km from the bulk of the data in their sampled sections. Here, we present an assessment of evaporative overprinting of primary water signatures in these siderites. We interpret the siderites as evaporatively enriched, and we report the mean elevation estimates of

each formation focusing on preserved primary oxygen values.

Evaporative re-enrichment of $\delta^{18}\text{O}_w$, as recorded by $\delta^{18}\text{O}_c$, is particularly prevalent in carbonates formed in closed lakes and some groundwater systems (Steinman et al., 2013). The covariance of oxygen and hydrogen isotopes of meteoric water usually follows the established global meteoric water line (GMWL; Friedman, 1953; Rozanski et al., 1993). However, fast evaporation causes a kinetic isotope effect that disturbs this trend, with a greater effect on the oxygen isotopes (Craig, 1961). The "evaporative slope," or trajectory off the GMWL, is determined by local relative humidity and temperature (Clark and Fritz, 1997). Polissar et al. (2009), using combined $\delta^{18}\text{O}$ and δD of samples from the Lunpola Basin, were able to corroborate the interpretation of Rowley and Currie (2006) that variable evaporative enrichment was the primary control on the isotopic composition of their samples. Polissar et al. (2009) thereby provided independent support for the use of the more negative oxygen-isotope compositions for the purposes of paleoaltimetry.

Oiyug Basin localities 618 (Upper Gazhacun Formation) and 621 (Oiyug Formation) provide both $\delta^{18}\text{O}$ and δD (from carbonates and organics, respectively), allowing us to plot these samples relative to the long-term precipitation amount-weighted mean GMWL ($\delta\text{D} = 8.20 \times \delta^{18}\text{O} + 11.27$; Rozanski et al., 1993). We correlated $\delta^{18}\text{O}_w$ and δD_w using the GMWL in order to compare relative isotopic enrichment of different materials within the same sedimentary horizons (618 or 621; Fig. A2 [see footnote 1]). Calcite-derived surface-water oxygen-isotope compositions from the 621 horizon were isotopically lighter than their corresponding δD values, calculated from coeval leaf waxes. Very low $\delta^{18}\text{O}_w$ could indicate diagenesis, but because both calcites retain primary Δ_{47} -derived temperatures, we can rule out the possibility of excessive alteration. However, the two siderites from the 618 and 621 localities yielded $\delta^{18}\text{O}_w$ estimates that are $\sim 4\%$ – 10% higher than expected from δD values of coeval leaf waxes. Based on the observation that the calcites from these localities appear to preserve primary $\delta^{18}\text{O}_w$ values, we interpret the ^{18}O -enriched siderites to be the product of groundwater evaporation. This suggests that any estimated water $\delta^{18}\text{O}$ compositions from this section with values $> -20\%$ are likely evaporatively ^{18}O -enriched values. We followed this approach by stressing elevation estimates based on the more ^{18}O -depleted compositions under the assumption that more-enriched values reflect more extensive evaporative re-enrichment relative to precipitation (Clark and Fritz, 1997).

CENOZOIC CLIMATE

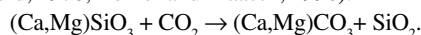
Reported $T(\Delta_{47})$ values (Table 3) are likely warmer than mean annual air temperature (MAAT) due to the nature of increased carbonate precipitation in the warm months in both soils and lake settings (Quade et al., 2013; Huntington et al., 2010). $T(\Delta_{47})$ therefore likely describes a warm-month temperature, June–July–August (JJA), for lake-derived sediments and a peak summer temperature for paleosols (Quade et al., 2013). Soil carbonate formation (due to CO_2 outgassing during groundwater evaporation) is most prevalent in the summer due to incident sunlight warming the uppermost 25 cm of soil. Lacustrine carbonate formation occurs in warm, unmixed near-surface waters. Here, abundant sunlight supports photosynthetic carbon fixation, which in turn can drive calcite and aragonite supersaturation by increasing pH and providing carbonate nucleation sites (Stumm and Morgan, 1981). For the purpose of both isotopic and temperature lapse rates in calculating paleoelevations, reporting warmer temperatures than MAAT assures a conservative estimate of paleoelevation.

The increased evaporative signal seen in the middle Gazhacun lake sediments could indicate a paleoenvironmental change, such as shallower, potentially closed playa lakes in this region in the mid-Miocene, or a paleoclimatic change, such as warmer temperatures, decreased humidity, or changes in atmospheric circulation injecting drier air masses. The lacustrine dolomites from the Badamaqen section are stratigraphically closest to clumped-isotope sample 555 with a $T(\Delta_{47})$ value of 19.7 ± 4.2 °C (\pm s.e.m.). However, the lacustrine calcites, 551 and 553, are temporally bracketed by clumped-isotope samples 554B and 548 with $T(\Delta_{47})$ values of 3.9 ± 3.4 °C and 7.6 ± 3.3 °C, respectively. Khan et al. (2014) used the Climate Leaf Analysis Multivariate Program (CLAMP) on a ca. 15 Ma fossil flora from this region to estimate a WMMT of 8.8 °C and cold month mean temperature (CMMT) of -6 ± 4 °C for the Oiyug Basin. Sample 555 did not provide enough evidence to suggest that the mean temperature of the Oiyug Basin was significantly warmer during the mid-Miocene. The evaporative enrichment signal, preserved as a shift to higher $\delta^{18}\text{O}$ values in lake sediments, can likely be attributed to shallow playa lake morphology. However, shifts in regional climate and atmospheric circulation should also be considered.

Tectonic-Weathering-Climate Feedbacks

Himalayan paleoaltimetry, or more specifically, the timing of the rise of the Himalaya,

has figured prominently in attempts to connect global cooling during the Cenozoic with continental weathering rates and $p\text{CO}_2$ (Ruddiman and Kutzbach, 1989; Raymo and Ruddiman, 1992; Harrison et al., 1992; Kutzbach et al., 1989; Molnar et al., 1993). Cenozoic cooling is documented most thoroughly in the $\delta^{18}\text{O}$ records of benthic foraminifers (e.g., Zachos et al., 2001). The potential for a connection between global climate and weathering is forged through the central role of CO_2 as both a greenhouse gas and chemical weathering agent (e.g., Kump et al., 2000). The chemical weathering of silicate and aluminosilicate rocks consumes CO_2 as carbonic acid, exporting cations and carbonate alkalinity to the oceans, where both are removed as carbonate minerals with generic overall reactions (e.g., Ebelmen, 1845; Urey, 1952; Holland, 1978; Berner and Maasch, 1996):



This type of chemical weathering serves as a net sink for atmospheric CO_2 . Raymo et al. (1988) and Raymo and Ruddiman (1992) suggested that uplift of the Himalaya could have enhanced chemical weathering rates by increasing the surface area of aluminosilicates available to weather. This surface area generation resulted from physical erosion processes that were accelerated by relief and glacial activity.

Evidence for the temporal link between the rise of the Himalaya and shifts in global weathering fluxes has relied heavily on the marine Sr isotope record. Sr has a long residence time in the oceans and is well mixed in terms of concentration and isotopic composition. Marine carbonates record the $^{87}\text{Sr}/^{86}\text{Sr}$ ratio of ambient seawater. The marine Sr isotope record is strongly influenced by the weathering flux of Sr to the oceans, and therefore it is used as a weathering proxy (e.g., Richter et al., 1992; Edmond, 1992). Shifts in the marine $^{87}\text{Sr}/^{86}\text{Sr}$ record over the Cenozoic appeared to coincide with earlier estimates for the timing of the uplift of the Himalaya (e.g., Raymo and Ruddiman, 1992; Richter et al., 1992). Furthermore, modern-day weathering of highly radiogenic terrains in the Himalaya provides a large flux of radiogenic Sr to the ocean, contributing to the continuing rise in the $^{87}\text{Sr}/^{86}\text{Sr}$ ratio of seawater and consistent with overall Neogene trends (Palmer and Edmond, 1989, 1992; Galy et al., 1999).

Large changes in the Sr isotopic composition of the oceans from the late Eocene through present are invoked to signify the onset and importance of weathering of the Himalaya and Tibet. By extension, this curve is often cited as an indication that significant topography first developed during the India-Eurasia collision at roughly 38 Ma (e.g., Raymo and Ruddiman, 1992; Misra and Froelich, 2012). Misra and

Froelich (2012) and others have argued that other proxies for chemical weathering rates and intensity of weathering, such as lithium isotopes, fit within this paradigm of the onset of Tibetan weathering in the late Eocene.

Our results provide strong evidence for high topography at the Tibetan margin dating to at least 56 Ma. This is well before the marine $^{87}\text{Sr}/^{86}\text{Sr}$ record begins its nearly monotonic climb toward more radiogenic values. Paleoaltitudes in the Linzizong arc had reached modern Tibetan elevations prior to the Paleocene-Eocene thermal maximum and overlapped with early Eocene equable climate states on Earth (Fig. 8). These high elevations were achieved at low latitudes (arc position roughly $19 \pm 4^\circ\text{N}$; van Hinsbergen et al., 2012) in warm and wet conditions favorable for intensive chemical weathering. All told, our paleoaltimetric findings suggest that enhanced chemical weathering of the high Linzizong arc was insufficient to provide significant climatic forcing, at least during the early and middle Eocene.

This does not rule out the possibility for enhanced weathering related to high topography along the southern Tibetan margin. The Linzizong arc was a source of highly reactive volcanic glasses and lithologies, i.e., andesite, dacite, and rhyolite, with some trachyandesite and basaltic trachyandesite (Mo et al., 2008). Weathering of the Linzizong arc would have delivered rather nonradiogenic Sr to the oceans. The $^{87}\text{Sr}/^{86}\text{Sr}$ of relict volcanic arcs dating to that interval is generally between 0.7045 and 0.7075 (Mo et al., 2008). If the Linzizong arc became globally significant in terms of supplying weathered Sr to the oceans, the resultant Sr flux would not have shifted marine $^{87}\text{Sr}/^{86}\text{Sr}$ appreciably from its value of 0.7078 in the early Eocene.

Even if there were enhanced chemical weathering associated with the early development of high elevation in the Linzizong arc, the overall carbon cycle dynamics associated with tectonism would remain complicated. Uplift and arc volcanism can be associated with enhanced outgassing of metamorphic and volcanic CO_2 (e.g., Kerrick and Caldeira, 1993), which could counteract or even reverse the carbon balance in such a setting. If organic-rich marine sediments were also exposed, then oxidative weathering of the organics would have served as an additional CO_2 source to the atmosphere (e.g., Beck et al., 1995). On the other hand, carbon sinks linked to tectonism include the potential for enhanced organic carbon burial efficiency through rapid burial rates in submarine fans and the high flux of fine-grained sediments to the oceans with subsequent mineral surface area control on organic matter burial (e.g., Hedges and Keil, 1995; France-Lanord and Derry, 1997; Galy et al.,

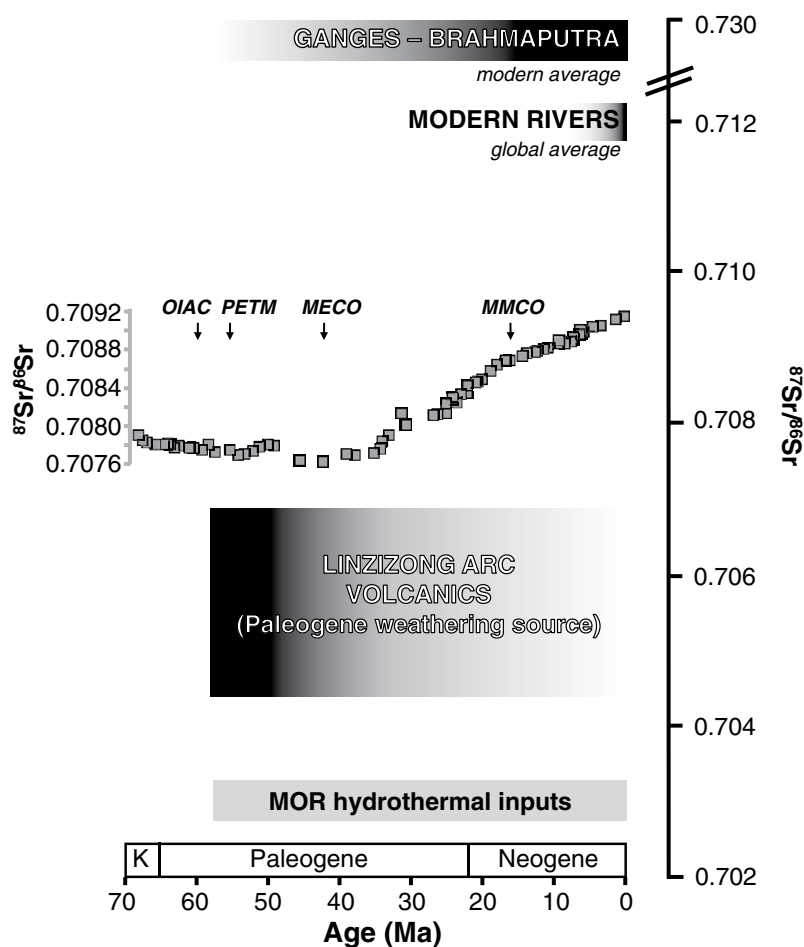


Figure 8. Cenozoic marine Sr isotope record in relation to source flux compositions. The major feature of the Cenozoic record of seawater $^{87}\text{Sr}/^{86}\text{Sr}$ (plotted here using measured values on planktonic foraminifers; Misra and Froelich, 2012) is the steep climb in ratios from roughly 38–36 Ma to present. This is conventionally interpreted as reflecting the onset of uplift in the India-Eurasia collision system, with chemical weathering of radiogenic terrains (e.g., Raymo and Ruddiman, 1992; Richter et al., 1992). The modern-day isotopic composition of the Ganges-Brahmaputra dissolved Sr flux is sufficiently high (e.g., Palmer and Edmond, 1992; Galy et al., 1999; indicated on schematic) and sufficiently large that it shifts the modern global average river input flux to high $^{87}\text{Sr}/^{86}\text{Sr}$ ratios (e.g., Edmond, 1992). This sustains the marine $^{87}\text{Sr}/^{86}\text{Sr}$ ratio at elevated values relative to the Paleogene. Our results indicate that the Linzizong arc was already at modern elevations in the late Paleocene and early Eocene. If chemical weathering rates were accelerated in these early stages of India-Eurasia collision, they likely would not have exerted significant influence on the marine Sr isotope record, because the arc lithologies had relatively non-radiogenic isotopic compositions (Mo et al., 2008). Major Cenozoic climate and tectonic events are marked with arrows: onset of India-Asia collision (OIAC), Paleocene-Eocene thermal maximum (PETM), mid-Eocene climatic optimum (MECO), and mid-Miocene climatic optimum (MMCO). MOR—mid-ocean ridge; K—Cretaceous.

2007). Organic carbon burial rates could also be influenced by changes in nutrient fluxes to the ocean as the rates and relative importance of different weathering domains and marine depositional environments changed (Compton and Mallinson, 1996; Colman and Holland, 2000). Finally, the overall carbon mass balance for the atmosphere-ocean system likewise links to carbon release from mid-ocean-ridge (MOR) spreading centers, and thus to global tectonism, which may or may not be coupled to regional processes (Richter et al., 1992).

Our results provide strong evidence that the marine Sr isotope record is not a sensitive indicator for the early rise of the Tibetan margin nor for the impact that the development of this topography had on global chemical weathering rates. The fact that this topography developed during a time of globally warm climates suggests that any enhancement in chemical weathering rates, which would have tended to lower atmospheric CO_2 , was offset by other features and feedbacks in the global carbon cycle.

CONCLUSIONS

We reconstructed an elevation history from the Tibetan Plateau spanning nearly the entire Cenozoic, from the onset of India-Asia collision to the present. This study provides multiple lines of geochemical evidence that the southern margin of the Lhasa block was at modern elevation or higher (4 to >5 km) around the onset of collision at ca. 55 Ma. In particular, carbonate clumped isotopes provide a new dimension to previous paleoelevation reconstructions of the southern Lhasa terrane. Additionally, the Paleocene–Eocene carbonates of the Penbo Basin provide apparent evidence that clumped-isotope values can survive substantial burial and heating. This result underscores the importance of detail and persistence in using isotopic proxies in studies of past climate and tectonics.

We find that both temperature lapse rates, informed by our clumped-isotope measurements, and traditional stable-isotope lapse rates of paleoprecipitation, informed by oxygen-isotope compositions of lacustrine and pedogenic carbonates, agree that the sediments associated with the Linzizong volcanic arc are in reasonable accord with the “Lhasaplano” model of tectonic evolution. Further work on the central and northern plateau is necessary in order to differentiate between a preexisting Andean-type volcanic arc and a more extensive high terrain such as a protoplateau in the early Cenozoic. Additionally, our data indicate high topography at low latitude dating to before the Eocene climatic optimum, suggesting more complicated linkages among the Himalayan orogeny, proxies

for chemical weathering, and tectonics, weathering, and climate.

ACKNOWLEDGMENTS

We thank R. Plotnick and K. Ritterbush for assistance with petrographic analyses, B. He for assistance with clumped-isotope measurements, and D. Schrag and S. Bernasconi for providing carbonate isotopic standards. Ingalls would like to thank Madison Ball and Xu Qiang for assistance in the field. The science and structure of this work were greatly improved by thoughtful reviews by D. Orme and J. Quade, and comments from *GSA Bulletin* Editor B. Singer. This work was supported by National Science Foundation grant EAR-0609756 awarded to Currie and grant EAR-111274 awarded to Rowley and Shuster, and a Geological Society of America Graduate Student Research Grant to Ingalls. Geochemical analyses were enabled by National Science Foundation grant EAR-0923831 awarded to Colman and Rowley.

REFERENCES CITED

- Barker, C.E., 1988, Geothermics of petroleum systems: Implications of the stabilization of kerogen thermal maturation after a geologically brief heating duration at peak temperature, in Magoon, L.B., ed., *Petroleum Systems of the United States*: U.S. Geological Survey Bulletin 1870, p. 26–29.
- Beck, R.A., Burbank, D.W., Sercombe, W.J., Riley, G.W., Barndt, J.K., Berry, J.R., Afzal, J., Khan, A.M., Jurgen, H., Metje, J., Cheema, A., Shafique, N.A., Lawrence, R.D., and Khan, M.A., 1995, Stratigraphic evidence for an early collision between northwest India and Asia: *Nature*, v. 373, p. 55–58, doi:10.1038/373055a0.
- Berner, R., and Maasch, K., 1996, Chemical weathering and controls on atmospheric O₂ and CO₂: Fundamental principles were enunciated by J.J. Ebelman in 1845: *Geochimica et Cosmochimica Acta*, v. 60, p. 1633–1637, doi:10.1016/0016-7037(96)00104-4.
- Burg, J.-P., Proust, F., Tapponnier, P., and Chen, G.M., 1983, Deformation phases and tectonic evolution of the Lhasa block (southern Tibet, China): *Eclogae Geologicae Helvetiae*, v. 76, p. 643–665.
- Burgener, L., Huntington, K.W., Hoke, G.D., Schauer, A., Ringham, M.C., Latorre, C., and Diaz, F.P., 2016, Variations in soil carbonate formation and seasonal bias over ~4 km of relief in the western Andes (30°S) revealed by clumped isotope thermometry: *Earth and Planetary Science Letters*, v. 441, p. 188–199, doi:10.1016/j.epsl.2016.02.033.
- Chen, H., Han, J., Ding, Z., Sun, H., and Guo, Z., 2008, Chronological dating and tectonic implications of late Cenozoic volcanic rocks and lacustrine sequence in Oiyug Basin of southern Tibet: *Science in China*, ser. D, v. 51, p. 275–283, doi:10.1007/s11430-008-0007-6.
- Clark, I., and Fritz, P., 1997, *Environmental Isotopes in Hydrogeology*: Boca Raton, Florida, Lewis Publishers, 342 p.
- Colman, A.S., and Holland, H., 2000, The global diagenetic flux of phosphorus from marine sediments to oceans: Redox sensitivity and the control of atmospheric oxygen levels, in Glenn, C.R., Prévôt, L., and Lucas, J., eds., *Marine Authigenesis: From Global to Microbial: Society for Sedimentary Geology (SEPM) Special Publication 66*, p. 53–75.
- Compton, J., and Mallinson, D., 1996, Geochemical consequences of increased late Cenozoic weathering rates and the global CO₂ balance since 100 Ma: *Paleoceanography*, v. 11, p. 431–446.
- Coplen, T., Brand, W., Gehre, M., Groning, M., Meijer, H., Toman, B., and Verkoouteren, R., 2006, New guidelines for $\delta^{13}\text{C}$ measurements: *Analytical Chemistry*, v. 78, p. 2439–2441, doi:10.1021/ac052027c.
- Craig, H., 1961, Isotopic variations in meteoric waters: *Science*, v. 133, p. 1702–1703, doi:10.1126/science.133.3465.1702.
- Currie, B.S., Rowley, D.B., and Tabor, N.J., 2005, Middle Miocene paleoaltimetry of southern Tibet: Implications for the role of mantle thickening and delamination in the Himalayan orogen: *Geology*, v. 33, p. 181–184, doi:10.1130/G21170.1.
- Currie, B.S., Polissar, P.J., Rowley, D.B., Ingalls, M., Li, S., and Freeman, K.H., 2016, Multiproxy paleoaltimetry of the late Oligocene–Pliocene Oiyug Basin, southern Tibet: *American Journal of Science*, v. 316, p. 401–436, doi:10.2475/05.2016.01.
- Dansgaard, W., 1954, The O¹⁸ abundance in fresh water: *Geochimica et Cosmochimica Acta*, v. 6, p. 241–260, doi:10.1016/0016-7037(54)90003-4.
- DeCelles, P.G., Quade, J., Kapp, P., Fan, M., Dettman, D.L., and Ding, L., 2007, High and dry in central Tibet during the late Oligocene: *Earth and Planetary Science Letters*, v. 253, p. 389–401, doi:10.1016/j.epsl.2006.11.001.
- DeCelles, P.G., Kapp, P., Quade, J., and Gehrels, G.E., 2011, Oligocene–Miocene Kailas Basin, southwestern Tibet: Record of postcollisional upper-plate extension in the Indus–Yarlung suture zone: *Geological Society of America Bulletin*, v. 123, p. 1337–1362, doi:10.1130/B30258.1.
- DeCelles, P.G., Kapp, P., Gehrels, G., and Ding, L., 2014, Paleocene–Eocene foreland basin evolution in the Himalaya of southern Tibet and Nepal: Implications for the age of initial India–Asia collision: *Tectonics*, v. 33, p. 824–849, doi:10.1002/2014TC003522.
- Defliese, W.F., Hren, M.T., and Lohmann, K.C., 2015, Compositional and temperature effects of phosphoric acid fractionation on $\Delta 47$ analysis and implications for discrepant calibrations: *Chemical Geology*, v. 396, p. 51–60, doi:10.1016/j.chemgeo.2014.12.018.
- Dennis, K., Affek, H., Passey, B., Schrag, D., and Eiler, J., 2011, Defining an absolute reference frame for “clumped” isotope studies of CO₂: *Geochimica et Cosmochimica Acta*, v. 75, p. 7117–7131, doi:10.1016/j.gca.2011.09.025.
- Ding, L., and Lai, Q., 2003, New geological evidence of crustal thickening in the Gangdese block prior to the Indo-Asian collision: *Chinese Science Bulletin*, v. 48, p. 1604–1610, doi:10.1007/BF03183969.
- Ding, L., Xu, Q., Yue, Y., Wang, H., Cai, F., and Li, S., 2014, The Andean-type Gangdese Mountains: Paleoelevation record from the Paleocene–Eocene Linzhou Basin: *Earth and Planetary Science Letters*, v. 392, p. 250–264, doi:10.1016/j.epsl.2014.01.045.
- Ding, L., Spicer, R.A., Yang, J., Xu, Q., Cai, Q., Li, S., Lai, Q., Wang, H., Spicer, T.E.V., Yue, Y., Shukla, A., Srivastava, G., Ali Khan, M., Bera, S., et al., 2017, Quantifying the rise of the Himalaya orogen and implications for the South Asian monsoon: *Geology*, v. 45, no. 3, p. 215–218, doi:10.1130/G38583.1.
- Ebelman, J., 1845, Sur les produits de la decomposition des especes minerales de la famille des silicates: *Annales des Mines*, v. 7, p. 3–66.
- Edmond, J.M., 1992, Himalayan tectonics, weathering processes, and the strontium isotope record in marine limestones: *Science*, v. 258, p. 1594–1597, doi:10.1126/science.258.5088.1594.
- Eiler, J.M., 2007, “Clumped-isotope” geochemistry—The study of naturally-occurring, multiply-substituted isotopologues: *Earth and Planetary Science Letters*, v. 262, p. 309–327, doi:10.1016/j.epsl.2007.08.020.
- England, P., and Houseman, G., 1986, Finite strain calculations of continental deformation: 2. Comparison with the India–Asia collision zone: *Journal of Geophysical Research*, v. 91, p. 3664–3676, doi:10.1029/JB091iB03p03664.
- Farley, K.A., Wolf, R.A., and Silver, L.T., 1996, The effects of long alpha-stopping distances on (U–Th)/He ages: *Geochimica et Cosmochimica Acta*, v. 60, p. 4223–4229, doi:10.1016/S0016-7037(96)00193-7.
- France-Lanord, C., and Derry, L., 1997, Organic carbon burial forcing of the carbon cycle from Himalayan erosion: *Nature*, v. 390, p. 65–67, doi:10.1038/36324.
- Friedman, I., 1953, Deuterium content of natural waters and other substances: *Geochimica et Cosmochimica Acta*, v. 4, p. 89–103, doi:10.1016/0016-7037(53)90066-0.
- Gaetani, M., and Garzanti, E., 1991, Multicyclic history of the northern India continental margin (northwestern Himalaya): *American Association of Petroleum Geologists Bulletin*, v. 75, p. 1427–1446.
- Gallagher, T.M., and Sheldon, N.D., 2016, Combining soil water balance and clumped isotopes to understand the nature and timing of pedogenic carbonate formation: *Chemical Geology*, v. 435, p. 79–91, doi:10.1016/j.chemgeo.2016.04.023.
- Galy, A., France-Lanord, C., and Derry, L., 1999, The strontium isotopic budget of Himalayan rivers in Nepal and Bangladesh: *Geochimica et Cosmochimica Acta*, v. 63, p. 1905–1925, doi:10.1016/S0016-7037(99)00081-2.
- Galy, A., France-Lanord, C., Beyssac, O., Faure, P., Kudrass, H., and Palhol, F., 2007, Efficient organic carbon burial in the Bengal fan sustained by the Himalayan erosional system: *Nature*, v. 450, p. 407–410, doi:10.1038/nature06273.
- Garzzone, C.N., Dettman, D.L., Quade, J., DeCelles, P.G., and Butler, R.F., 2000, High times on the Tibetan Plateau: Paleoelevation of the Thakkhola graben, Nepal: *Geology*, v. 28, p. 339–342, doi:10.1130/0091-7613(2000)28<339:HTOTTP>2.0.CO;2.
- Garzzone, C.N., Dettman, D.L., and Horton, B.K., 2004, Carbonate oxygen isotope paleoelevation: Evaluating the effect of diagenesis on paleoelevation estimates for the Tibetan Plateau: *Palaeogeography, Palaeoclimatology, Palaeoecology*, v. 212, p. 119–140, doi:10.1016/S0031-0182(04)00307-4.
- Gébelin, A., Mulch, A., Teysseier, C., Jessup, M.J., Law, R.D., and Brunel, M., 2013, The Miocene elevation of Mount Everest: *Geology*, v. 41, p. 799–802, doi:10.1130/G34331.1.
- Ghosh, P., Adkins, J., Affek, H., Balta, B., Guo, W.W., Schauble, E.E.A., Schrag, D., Eller, J., and Eiler, J.M., 2006a, ¹³C–¹⁸O bonds in carbonate minerals: A new kind of paleothermometer: *Geochimica et Cosmochimica Acta*, v. 70, p. 1439–1456, doi:10.1016/j.gca.2005.11.014.
- Ghosh, P., Garzzone, C.N., and Eiler, J.M., 2006b, Rapid uplift of the Altiplano revealed through ¹³C–¹⁸O bonds in paleosol carbonates: *Science*, v. 311, p. 511–515, doi:10.1126/science.1119365.
- Gonfiantini, R., 1983, Advisory Group Meeting on Stable Isotope Reference Samples for geochemical and Hydrological Investigations: Report to the Director General: Vienna, Austria, International Atomic Energy Agency (IAEA), 77 p.
- Green, O.R., Searle, M.P., Corfield, R.I., and Corfield, R.M., 2008, Cretaceous–Tertiary carbonate platform evolution and the age of the India–Asia collision along the Ladakh Himalaya (northwest India): *The Journal of Geology*, v. 116, p. 331–353, doi:10.1086/588831.
- Harrison, T.M., Copeland, P., Kidd, W.S., and Yin, A., 1992, Raising Tibet: *Science*, v. 255, p. 1663–1670, doi:10.1126/science.255.5052.1663.
- Harrison, T.M., Copeland, P., Kidd, W.S.F., and Lovera, O.M., 1995, Activation of the Nyainqentanghla shear zone: Implications for uplift of the southern Tibetan Plateau: *Tectonics*, v. 14, p. 658–676.
- He, B., Olack, G., and Colman, A., 2012, Pressure baseline correction and high-precision CO₂ clumped-isotope ($\Delta 47$) measurements in bellows and micro-volume modes: *Rapid Communications in Mass Spectrometry*, v. 26, p. 2837–2853, doi:10.1002/rcm.6436.
- He, S., Kapp, P., DeCelles, P.G., Gehrels, G.E., and Heizer, M., 2007, Cretaceous–Tertiary geology of the Gangdese arc in the Linzhou area, southern Tibet: *Tectonophysics*, v. 433, p. 15–37, doi:10.1016/j.tecto.2007.01.005.
- Hedges, J., and Keil, R., 1995, Sedimentary organic matter preservation: An assessment and speculative synthesis: *Marine Chemistry*, v. 49, p. 81–115, doi:10.1016/0304-4203(95)00008-F.
- Henkes, G.A., Passey, B.H., Grossman, E.L., Shenton, B.J., Perez-Huerta, A., and Yancey, T.E., 2014, Temperature limits for preservation of primary calcite clumped isotope paleotemperatures: *Geochimica et Cosmochimica Acta*, v. 139, p. 362–382, doi:10.1016/j.gca.2014.04.040.
- Hoke, G.D., Liu-Zeng, J., Hren, M.T., Wissink, G.K., and Garzzone, C.N., 2014, Stable isotopes reveal high southeast Tibetan Plateau margin since the Paleogene: *Earth and Planetary Science Letters*, v. 394, p. 270–278, doi:10.1016/j.epsl.2014.03.007.

- Holland, H., 1978, *The Chemistry of the Atmosphere and Oceans*: New York, Wiley, 351 p.
- Hough, B., Fan, M., and Passey, B., 2014, Calibration of the clumped isotope geothermometer in soil carbonate in Wyoming and Nebraska, USA: Implications for paleoelevation and paleoclimate reconstruction: *Earth and Planetary Science Letters*, v. 391, p. 110–120, doi:10.1016/j.epsl.2014.01.008.
- Hren, M.T., Bookhagen, B., Blisniuk, P.M., Booth, A.L., and Chamberlain, C.P., 2009, $\delta^{18}\text{O}$ and δD of streamwaters across the Himalaya and Tibetan Plateau: Implications for moisture sources and paleoelevation reconstructions: *Earth and Planetary Science Letters*, v. 288, p. 20–32, doi:10.1016/j.epsl.2009.08.041.
- Hu, X., Garzanti, E., Moore, T., and Raffi, I., 2015, Direct stratigraphic dating of India-Asia collision onset at the Selandian (middle Paleocene, 59 ± 1 Ma): *Geology*, v. 43, p. 859–862, doi:10.1130/G36872.1.
- Huntington, K.W., Eiler, J.M., Affek, H.P., Guo, W., Bonifacie, M., Yeung, L.Y., Thiagarajan, N., Passey, B., Tripati, A., Daëron, M., and Came, R., 2009, Methods and limitations of “clumped” CO_2 isotope ($\Delta 47$) analysis by gas-source isotope ratio mass spectrometry: *Journal of Mass Spectrometry*, v. 44, p. 1318–1329, doi:10.1002/jms.1614.
- Huntington, K.W., Wernicke, B.P., and Eiler, J.M., 2010, Influence of climate change and uplift on Colorado Plateau paleotemperatures from carbonate clumped isotope thermometry: *Tectonics*, v. 29, TC3005, doi:10.1029/2009TC002449.
- Huntington, K.W., Saylor, J., Quade, J., and Hudson, A.M., 2015, High late Miocene–Pliocene elevation of the Zhada Basin, southwestern Tibetan Plateau, from carbonate clumped isotope thermometry: *Geological Society of America Bulletin*, v. 127, p. 181–199, doi:10.1130/B31000.1.
- Ingalls, M., 2017, Subduction and Uplift of Continental Crust in the India-Asia Collision Zone: Clumped-Isotope Paleothermometry and Paleoclimatology of the Lhasa Block, Southern Tibet [Ph.D. dissertation]: Chicago, Illinois, University of Chicago, 250 p.
- Ingalls, M., Rowley, D.B., Currie, B., and Colman, A.S., 2016, Large-scale subduction of continental crust implied by India-Asia mass-balance calculation: *Nature Geoscience*, v. 9, p. 848–853, doi:10.1038/ngeo2806.
- Kalnay, E., Kanamitsu, M., Kistler, R., Collins, W., Deaven, D., Gandin, L., Iredell, M., Saha, S., White, G., Woollen, J., Zhu, Y., Chelliah, M., Ebisuzaki, W., Higgins, W., et al., 1996, The NCEP/NCAR 40-Year Reanalysis Project: *Bulletin of the American Meteorological Society*, v. 77, p. 437–471, doi:10.1175/1520-0477(1996)077<0437:TNYRP>2.0.CO;2.
- Kapp, P., Yin, A., Harrison, T.M., and Ding, L., 2005, Cretaceous–Tertiary shortening, basin development, and volcanism in central Tibet: *Geological Society of America Bulletin*, v. 117, p. 865–878, doi:10.1130/B25595.1.
- Kapp, P., DeCelles, P.G., Leier, A.L., Fabjanic, J.M., He, S., Pullen, A., Gehrels, G.E., and Ding, L., 2007, The Gangdese retroarc thrust belt revealed: *GSA Today*, v. 17, p. 4–9, doi:10.1130/GSAT01707A.1.
- Kerrick, D., and Caldeira, K., 1993, Paleotemperature consequences of CO_2 released during early Cenozoic regional metamorphism in the Tethyan orogen: *Chemical Geology*, v. 108, p. 201–230, doi:10.1016/0009-2541(93)90325-D.
- Khan, M.A., Spicer, R.A., Bera, S., Ghosh, R., Yang, J., Spicer, T.E.V., Guo, S., Su, T., Jacques, F., and Grote, P.J., 2014, Miocene to Pleistocene floras and climate of the Eastern Himalayan Siwaliks, and new paleoelevation estimates for the Namling–Oiyug Basin, Tibet: *Global and Planetary Change*, v. 113, p. 1–10, doi:10.1016/j.gloplacha.2013.12.003.
- Kim, S., and O’Neil, J., 1997, Equilibrium and nonequilibrium oxygen isotope effects in synthetic carbonates: *Geochimica et Cosmochimica Acta*, v. 61, no. 16, p. 3461–3475, doi:10.1016/S0016-7037(97)00169-5.
- Koppers, A.A.P., 2002, ArArCALC—Software for Ar-40/Ar-39 age calculations: *Computers & Geosciences*, v. 28, p. 605–619, doi:10.1016/S0098-3004(01)00095-4.
- Kump, L., Brantley, S., and Arthur, M., 2000, Chemical weathering, atmospheric CO_2 , and climate: A Review of Earth and Planetary Sciences, v. 28, p. 611–667, doi:10.1146/annurev.earth.28.1.611.
- Kutzbach, J.E., Guetter, P.J., Ruddiman, W.F., and Prell, W.L., 1989, Sensitivity of climate to late Cenozoic uplift in southern Asia and the American West: Numerical experiments: *Journal of Geophysical Research*, v. 94, p. 18393, doi:10.1029/JD094I15p18393.
- Lawrimore, J.H., Menne, M.J., Gleason, B.E., Williams, C.N., Wuertz, D.B., Vose, R.S., and Rennie, J., 2011, An overview of the Global Historical Climatology Network monthly mean temperature data set, version 3: *Journal of Geophysical Research*, v. 116, D19121, doi:10.1029/2011JD016187.
- Leary, R.J., Quade, J., DeCelles, P.G., and Reynolds, A., 2017, Evidence from paleosols for low to moderate elevation of the India-Asia suture zone during mid-Cenozoic time: *Geology*, v. 45, no. 5, p. 399–402, doi:10.1130/G38830.1.
- Leier, A., DeCelles, P.G., Kapp, P., and Ding, L., 2007, The Tarena Formation of the Lhasa terrane, southern Tibet: The record of a Late Cretaceous retroarc foreland basin: *Geological Society of America Bulletin*, v. 119, p. 31–48, doi:10.1130/B25974.1.
- Leier, A., Quade, J., DeCelles, P., and Kapp, P., 2009, Stable isotopic results from paleosol carbonate in South Asia: Paleoenvironmental reconstructions and selective alteration: *Earth and Planetary Science Letters*, v. 279, p. 242–254, doi:10.1016/j.epsl.2008.12.044.
- Le Pichon, X., Fournier, M., and Jolivet, L., 1992, Kinematics, topography, shortening, and extrusion in the India-Eurasia collision: *Tectonics*, v. 11, p. 1085–1098, doi:10.1029/92TC01566.
- Li, S., Currie, B.S., Rowley, D.B., and Ingalls, M., 2015, Cenozoic paleoaltimetry of the SE margin of the Tibetan Plateau: Constraints on the tectonic evolution of the region: *Earth and Planetary Science Letters*, v. 432, p. 415–424, doi:10.1016/j.epsl.2015.09.044.
- Machette, M.N., 1985, Calcic soils of the southwestern United States, in Weide, D.L., ed., *Soils and Quaternary Geology of the Southwestern United States*: Geological Society of America Special Paper 203, p. 1–21, doi:10.1130/SPE203-p1.
- Mack, G., and Rasmussen, K., 1984, Alluvial-fan sedimentation of the Cutler Formation (Permo-Pennsylvanian) near Gateway, Colorado: *Geological Society of America Bulletin*, v. 95, p. 109–116, doi:10.1130/0016-7606(1984)95<109:ASOTCF>2.0.CO;2.
- Misra, S., and Froelich, P.N., 2012, Lithium isotope history of Cenozoic seawater: Changes in silicate weathering and reverse weathering: *Science*, v. 335, p. 818–823, doi:10.1126/science.1214697.
- Mo, X.X., Niu, Y.L., Dong, G.C., Zhao, Z.D., Hou, Z.Q., Zhou, S., and Ke, S., 2008, Contribution of synclinal felsic magmatism to continental crustal growth: A case study of the Paleogene Lincizong volcanic succession in southern Tibet: *Chemical Geology*, v. 250, p. 49–67, doi:10.1016/j.chemgeo.2008.02.003.
- Molnar, P., England, P., and Martinod, J., 1993, Mantle dynamics, uplift of the Tibetan Plateau, and the Indian Monsoon: *Reviews of Geophysics*, v. 31, p. 357–396, doi:10.1029/93RG02030.
- Murphy, M.A., Yin, A., Harrison, T.M., Dürr, S.B., Chen Z., Ryerson, F.J., Kidd, W.S.F., Wang X., Zhou X., 1997, Did the Indo-Asian collision alone create the Tibetan Plateau?: *Geology*, v. 25, p. 719, doi:10.1130/0091-7613(1997)025<0719:DTIACA>2.3.CO;2.
- National Geological Archives of China (NGAC), 2002, Digital Library of NGAC Map H45C002003, <http://ngac.org.cn/onemap/index.html> (accessed June 2016).
- National Geological Archives of China (NGAC), 2012, Digital Library of NGAC Map H46C003001, <http://ngac.org.cn/onemap/index.html> (accessed June 2016).
- Orme, D.A., 2015, Basin Evolution and Exhumation of the Xigaze Forearc and Indus-Yarlung Suture Zone, Tibet [Ph.D. dissertation]: Tucson, Arizona, University of Arizona, 305 p.
- Palmer, M.R., and Edmond, J.M., 1989, The strontium isotope budget of the modern ocean: *Earth and Planetary Science Letters*, v. 92, p. 11–26, doi:10.1016/0012-821X(89)90017-4.
- Palmer, M.R., and Edmond, J.M., 1992, Controls over the strontium isotope composition of river water: *Geochimica et Cosmochimica Acta*, v. 56, p. 2099–2111, doi:10.1016/0016-7037(92)90332-D.
- Passey, B.H., Levin, N.E., Cerling, T.E., Brown, F.H., and Eiler, J.M., 2010, High-temperature environments of human evolution in East Africa based on bond ordering in paleosol carbonates: *Proceedings of the National Academy of Sciences of the United States of America*, v. 107, p. 11,245–11,249, doi:10.1073/pnas.1001824107.
- Pearson, P.N., Ditchfield, P.W., Singano, J., Harcourt-Brown, K.G., Nicholas, C.J., Olsson, R.K., Shackleton, N.J., and Hall, M.A., 2001, Warm tropical sea surface temperatures in the Late Cretaceous and Eocene Epochs: *Nature*, v. 413, p. 481–487, doi:10.1038/35097000.
- Peters, N.A., Huntington, K.W., and Hoke, G.D., 2013, Hot or not? Impact of seasonally variable soil carbonate formation on paleotemperature and O-isotope records from clumped isotope thermometry: *Earth and Planetary Science Letters*, v. 361, p. 208–218, doi:10.1016/j.epsl.2012.10.024.
- Polissar, P.J., Freeman, K.H., Rowley, D.B., McInerney, F.A., and Currie, B.S., 2009, Paleoaltimetry of the Tibetan Plateau from D/H ratios of lipid biomarkers: *Earth and Planetary Science Letters*, v. 287, p. 64–76, doi:10.1016/j.epsl.2009.07.037.
- Quade, J., and Cerling, T.E., 1995, Expansion of C4 grasses in the late Miocene of northern Pakistan: Evidence from stable isotopes in paleosols: *Palaeogeography, Palaeoclimatology, Palaeoecology*, v. 115, p. 91–116, doi:10.1016/0031-0182(94)00108-K.
- Quade, J., Cerling, T.E., and Bowman, J.R., 1989, Development of Asian monsoon revealed by marked ecological shift during the latest Miocene in northern Pakistan: *Nature*, v. 342, p. 163–166, doi:10.1038/342163a0.
- Quade, J., Cater, J.M.L., Ojha, T.P., Adam, J., and Mark Harrison, T., 1995, Late Miocene environmental change in Nepal and the northern Indian subcontinent: Stable isotopic evidence from paleosols: *Geological Society of America Bulletin*, v. 107, p. 1381–1397, doi:10.1130/0016-7606(1995)107<1381:LMECIN>2.3.CO;2.
- Quade, J., Garzzone, C., and Eiler, J., 2007, Paleoelevation reconstruction using pedogenic carbonates: Reviews in Mineralogy and Geochemistry, v. 66, p. 53–87, doi:10.2138/rmg.2007.66.3.
- Quade, J., Eiler, J., Daëron, M., and Achyuthan, H., 2013, The clumped isotope geothermometer in soil and paleosol carbonate: *Geochimica et Cosmochimica Acta*, v. 105, p. 92–107, doi:10.1016/j.gca.2012.11.031.
- Raymo, M., and Ruddiman, W., 1992, Tectonic forcing of late Cenozoic climate: *Nature*, v. 359, p. 117–122, doi:10.1038/359117a0.
- Raymo, M., Ruddiman, W., and Froelich, P.N., 1988, Influence of late Cenozoic mountain building on ocean geochemical cycles: *Geology*, v. 16, p. 649–653, doi:10.1130/0091-7613(1988)016<0649:IOLCMB>2.3.CO;2.
- Richter, F., Rowley, D., and DePaolo, D., 1992, Sr isotope evolution of seawater: The role of tectonics: *Earth and Planetary Science Letters*, v. 109, p. 11–23, doi:10.1016/0012-821X(92)90070-C.
- Ringham, M.C., Hoke, G.D., Huntington, K.W., and Aranibar, J.N., 2016, Influence of vegetation type and site-to-site variability on soil carbonate clumped isotope records, Andean piedmont of Central Argentina (32–34°S): *Earth and Planetary Science Letters*, v. 440, p. 1–11, doi:10.1016/j.epsl.2016.02.003.
- Rohrmann, A., Kapp, P., Carrapa, B., Reiners, P.W., Guynn, J., Ding, L., and Heizler, M., 2012, Thermochronologic evidence for plateau formation in central Tibet: By 45 Ma: *Geology*, v. 40, p. 187–190, doi:10.1130/G32530.1.
- Rowley, D.B., 2007, Stable isotope-based paleoaltimetry: Theory and validation: *Reviews in Mineralogy and Geochemistry*, v. 66, p. 23–52, doi:10.2138/rmg.2007.66.2.
- Rowley, D.B., and Currie, B.S., 2006, Palaeo-altimetry of the late Eocene to Miocene Lunpola Basin, central Tibet: *Nature*, v. 439, p. 677–681, doi:10.1038/nature04506.
- Rowley, D.B., and Garzzone, C.N., 2007, Stable isotope-based paleoaltimetry: A Annual Review of Earth and Planetary Sciences, v. 35, p. 463–508, doi:10.1146/annurev.earth.35.031306.140155.

- Rowley, D.B., Pierrehumbert, R.T., and Currie, B.S., 2001, A new approach to stable isotope-based paleoaltimetry: Implications for paleoaltimetry and paleohypsometry of the High Himalaya since the late Miocene: *Earth and Planetary Science Letters*, v. 188, no. 1-2, p. 253–268, doi:10.1016/S0012-821X(01)00324-7.
- Rowley, D.B., Currie, B.S., and Pierrehumbert, R.T., 2003, Modern precipitation stable isotope vs. elevation gradients in the High Himalaya [reply]: *Earth and Planetary Science Letters*, v. 209, p. 401–403, doi:10.1016/S0012-821X(03)00044-X.
- Rozanski, K., Araguas-Araguas, L., and Gonfiantini, R., 1993, Isotopic patterns in modern global precipitation, in *Climate Change in Continental Isotopic Records*: Washington, D.C., American Geophysical Union, p. 1–36, doi:10.1029/GM078p0001.
- Ruddiman, W.F., and Kutzbach, J.E., 1989, Forcing of late Cenozoic Northern Hemisphere climate by plateau uplift in southern Asia and the American West: *Journal of Geophysical Research*, v. 94, 18409, doi:10.1029/JD094iD15p18409.
- Saylor, J.E., Quade, J., Dettman, D.L., DeCelles, P.G., Kapp, P.A., and Ding, L., 2009, The late Miocene through present paleoelevation history of southwestern Tibet: *American Journal of Science*, v. 309, p. 1–42, doi:10.2475/01.2009.01.
- Spicer, R.A., Harris, N.B.W., Widdowson, M., Herman, A.B., Guo, S., Valdes, P.J., Wolfe, J.A., and Kelley, S.P., 2003, Constant elevation of southern Tibet over the past 15 million years: *Nature*, v. 421, p. 622–624, doi:10.1038/nature01356.
- Steinman, B.A., Abbott, M.B., Nelson, D.B., Stansell, N.D., Finney, B.P., Bain, D.J., and Rosenmeier, M.F., 2013, Isotopic and hydrologic responses of small, closed lakes to climate variability: Comparison of measured and modeled lake level and sediment core oxygen isotope records: *Geochimica et Cosmochimica Acta*, v. 105, p. 455–471, doi:10.1016/j.gca.2012.11.026.
- Stolper, D.A., and Eiler, J.M., 2015, The kinetics of solid-state isotope-exchange reactions for clumped isotopes: A study of inorganic calcites and apatites from natural and experimental samples: *American Journal of Science*, v. 315, p. 363–411, doi:10.2475/05.2015.01.
- Stumm, W., and Morgan, J.J., 1981, *Aquatic Chemistry: An Introduction Emphasizing Chemical Equilibria in Natural Waters*: New York, Wiley-Interscience, 583 p.
- Suarez, M.B., Passey, B.H., and Kaakinen, A., 2011, Paleosol carbonate multiple isotopologue signature of active East Asian summer monsoons during the late Miocene and Pliocene: *Geology*, v. 39, p. 1151–1154, doi:10.1130/G32350.1.
- Tapponnier, P., Mercier, J.L., Proust, F., Andrieux, J., Armijo, R., Bassoullet, J.P., Brunel, M., Burg, J.P., Colchen, M., Dupre, B., Girardeau, J., Marcoux, J., Mascle, G., Matte, P., et al., 1981, The Tibetan side of the India-Eurasia collision: *Nature*, v. 294, p. 405–410, doi:10.1038/294405a0.
- Tapponnier, P., Peltzer, G., and Armijo, R., 1986, On the mechanics of the collision between India and Asia, in Coward, M.P., and Ries, A.C., eds., *Collision Tectonics*: Geological Society of London Special Publication 19, p. 113–157, doi:10.1144/GSL.SP.1986.019.01.07.
- Tremblay, M., Fox, M., Schmidt, J.L., Tripathy-Lang, A., Wielicki, W., Harrison, T.M., Zeitler, P.K., and Shuster, D.L., 2015, Erosion in southern Tibet shut down at ~10 Ma due to enhanced rock uplift within the Himalaya: *Proceedings of the National Academy of Sciences of the United States of America*, v. 112, p. 12,030–12,035, doi:10.1073/pnas.1515652112.
- Urey, H., 1952, *The Planets: Their Origin and Development*: New Haven, Connecticut, Yale University Press, 245 p.
- van Hinsbergen, D.J.J., Lippert, P.C., Dupont-Nivet, G., McQuarrie, N., Doubrovine, P.V., Spakman, W., and Torsvik, T.H., 2012, Greater India Basin hypothesis and a two-stage Cenozoic collision between India and Asia: *Proceedings of the National Academy of Sciences of the United States of America*, v. 109, p. 7659–7664, doi:10.1073/pnas.1117262109.
- Vasconcelos, C., McKenzie, J.A., Warthmann, R., and Bernasconi, S.M., 2005, Calibration of the $\delta^{18}\text{O}$ paleothermometer for dolomite precipitated in microbial cultures and natural environments: *Geology*, v. 33, p. 317–320, doi:10.1130/G20992.1.
- Wang, C., Dai, J., Zhao, X., Li, Y., Graham, S.A., He, D., Ran, B., and Meng, J., 2014, Outward-growth of the Tibetan Plateau during the Cenozoic: A review: *Tectonophysics*, v. 621, p. 1–43, doi:10.1016/j.tecto.2014.01.036.
- Wang, J., and Chen, Y., 1999, Sedimentary formation characteristics of hydrocarbon generation and oil exploration prospects of Wuyu Basin in Tibet: *Petroleum Exploration and Development*, v. 26, p. 14–17 [in Chinese].
- Wang, Y., Deng, T., and Biasatti, D., 2006, Ancient diets indicate significant uplift of southern Tibet after ca. 7 Ma: *Geology*, v. 34, p. 309–312, doi:10.1130/G22254.1.
- Yue, Y., and Ding, L., 2006, Ar-40/Ar-39 geochronology, geochemical characteristics and genesis of the Linzhou basic dikes, Tibet: *Yanshi Xuebao*, v. 22, p. 855–866 [in Chinese].
- Zaarur, S., Affek, H.P., and Brandon, M.T., 2013, A revised calibration of the clumped isotope thermometer: *Earth and Planetary Science Letters*, v. 382, p. 47–57, doi:10.1016/j.epsl.2013.07.026.
- Zachos, J., Pagani, M., Sloan, L., Thomas, E., and Billups, K., 2001, Trends, rhythms, and aberrations in global climate 65 Ma to present: *Science*, v. 292, p. 686–693, doi:10.1126/science.1059412.
- Zhang, C.L., Horita, J., Cole, D.R., Zhou, J., Lovley, D.R., and Phelps, T.J., 2001, Temperature-dependent oxygen and carbon isotope fractionations of biogenic siderite: *Geochimica et Cosmochimica Acta*, v. 65, p. 2257–2271, doi:10.1016/S0016-7037(01)00596-8.
- Zhang, K.J., 2000, Cretaceous palaeogeography of Tibet and adjacent areas (China): Tectonic implications: *Cretaceous Research*, v. 21, p. 23–33, doi:10.1006/cres.2000.0199.
- Zhou, S., Mo, X.X., Zhao, Z.D., Qiu, R.Z., Niu, Y.L., Guo, T.Y., and Zhang, S.Q., 2010, Biosynthetic origin of the saw-toothed profile in $\delta^{13}\text{C}$ and δD of n-alkanes and systematic isotopic differences between n-, iso- and anteiso-alkanes in leaf waxes of land plants: *Journal of Asian Earth Sciences*, v. 37, p. 246–258, doi:10.1016/j.jseaes.2009.08.011.
- Zhu, Y., Fang, X., Gao, J., Yi, H., Wang, S., and Zhang, W., 2006, Oligo–Miocene depositional facies of the Wuyu Basin, southern Tibetan Plateau: *Acta Sedimentologica Sinica*, v. 24, p. 775–782.

SCIENCE EDITOR: BRADLEY S. SINGER
ASSOCIATE EDITOR: MICHAEL ELLIOT SMITH

MANUSCRIPT RECEIVED 12 DECEMBER 2016
REVISED MANUSCRIPT RECEIVED 18 MAY 2017
MANUSCRIPT ACCEPTED 12 JULY 2017

Printed in the USA